Topics on Electron, Neutrino and Axion Scattering

by

Prajwal Mohanmurthy

B.S. (Honors) Physics, Mississippi State University (2012)

Submitted to the Department of Physics
in partial fulfillment of the requirements for the degree of

Master of Science in Physics

at the

MASSACHUSETTS INSTITUTE OF TECHNOLOGY

September 2015

Author . . . .
Department of Physics
Aug 28, 2015

Certified by. . . . .
Joseph A. Formaggio
Associate Professor, MIT
Thesis Supervisor

Certified by. . . . .
Paul E. Reimer
Scientist, ANL
Thesis Supervisor

Accepted by . . . .
Richard G. Milner
Professor, MIT

Topics on Electron, Neutrino and Axion Scattering

by

Prajwal Mohanmurthy

Abstract

Under the broad topic of scattering, in this thesis we particularly investigate Lorentz invariance using Compton Scattering at the Compton Polarimeter located in Hall-C at Thomas Jefferson National Accelerator Facility. The Mississippi State Axion Search, an axion search experiment which uses light shining through a wall technique is described in detail, including its instrumentation, initial tests and future impact. Furthermore, a novel method of detection of solar anti-neutrinos based on coherent neutrino scattering is described. Additionally, on the instrumentation side, development of a multi-purpose beam instrument based on synchrotron light to measure the electron beam polarization, beam profile and intensity at the future Electron Ion Collider is presented.

Thesis Supervisor: Joseph A. Formaggio
Title: Associate Professor, MIT

Thesis Supervisor: Paul E. Reimer
Title: Scientist, ANL

Dedicated to,

all my past, present and future advisors and supervisors for having been their best when the goings have been tough.

Acknowledgments

Contents

Chapter 1

Test of Lorentz Invariance from Compton Scattering

$$e\gamma \rightarrow e\gamma$$

Abstract

In the recent times, test of Lorentz Invariance has been used as a means to probe theories of physics Beyond Standard Model (BSM), especially those such as extensions to String Theory and Quantum Gravity. Tests of Lorentz invariance could go a long way in setting the stage for possible theories which are beyond the standard model. We describe a simple way of utilizing electron polarimeters, which are a critical beam instrument at precision and intensity frontier nuclear physics labs such as Stanford Linear Accelerator Center (SLAC) and Thomas Jefferson National Accelerator Facility (JLab), to limit the dependence of speed of light with the energy of the photons. We also describe a way of limiting directional dependence of speed of light at previously unprecedented levels of precision by studying the sidereal variations. The method and preliminary results from this study as well as possible limits on Charge Parity Time (CPT) violating Standard Model Extension parameters will be presented.

1.1 Introduction

Lorentz invariance was first introduced in Special Relativity and then generalized in General Relativity to prevent infinities in self energies of Maxwellian Electro-Magnetic systems, but has formed the corner stone of modern standard model. Testing the Lorentz symmetry rigorously is thus a very interesting research activity. There are

direct tests of Lorentz invariance mostly involving studying the dependence of speed of light on a number of other physical properties such as its energy, over distance of propagation and direction of propagation, to name a few. According to the CPT theorem, the joint CPT symmetry has to hold for all processes governed by a Lorentz invariant theory and vice-versa [3]. Therefore, in particle and nuclear physics probing violations of CPT symmetry has been a means to test Lorentz invariance. Nuclear and particle physics methods often involve indirect tests of Lorentz invariance by measuring violations of CPT symmetry either by studying the joint CPT symmetry or by studying a subset of the CPT symmetry, such as CP symmetry violation or T symmetry violation independently.

Previous to the discovery of weak sector parity violation in beta decay experiment at NIST [1], it was assumed that parity was a conserved quantity. It was then assumed that CP was a conserved quantity until neutral kaon decay experiment proved otherwise [2]. Since then, CPT symmetry and Lorentz symmetry by extension, is shown to hold good in modern standard model. Certain BSM theories have however been known to break CPT symmetry and Lorentz symmetry by extension. Ref. [4] lists all known BSM theories that break CPT and Lorentz symmetry as of publication date, while Ref. [5] lists all the experimentally measured parameters limiting the violation of CPT and Lorentz symmetry as of publication date.

Compton scattering, which is currently the only way of continuously monitoring electron beam polarization precisely has spawned Compton polarimeters at each of the labs using polarized electron beam to probe nuclear matter such as SLAC and JLab. These Compton polarimeters have recently been demonstrated to achieve precision as low as 1% [6]. The high degree of precision of Compton polarimeters allows precise measurement of speed of light competent with the current leading limits. Using a competent value of the speed of light so obtained, limits on SME parameters could be established.

1.2   Compton Polarimeter

At JLab, the electron beam helicity ($\pm$) is switched at the rate of 960Hz and the photon beam used for Compton scattering can be switched on or off (on/off). A term, scattering asymmetry (A_{exp}) can then be defined by measuring the cross section of scattered electrons from Compton scattering.

$$A_{exp} = \frac{Y^+ - Y^-}{Y^+ + Y^-}$$
$$A_{exp} = P_\gamma P_e A_{phy} \tag{1.1}$$

where $Y^\pm = N_{on}^\pm/Q_{on}^\pm - N_{off}^\pm/Q_{off}^\pm$ so that backgrounds are subtracted when photon beam is turned off, $N_{on/off}^\pm$ is the cumulative number of scattered electrons detected at a strip and $Q_{on/off}^\pm$ is the cumulative main electron beam charge. P_γ is the polarization of the photons beam used and P_e is the polarization of the electron beam used. A_{phy}

is the physics asymmetry which can be calculated as a function of a dimensionless variable, ρ [34].

$$\rho = \frac{\omega'}{\omega_{max}} \approx \frac{\epsilon_0 - \epsilon'}{\epsilon_0 + \epsilon'_{min}} \qquad (1.2)$$

where ω' is the energy of the Compton scattered photon, ω_{max} is the maximum scattered photon energy, ϵ', ϵ'_{min} and ϵ_0 are scattered electron energy, minimum scattered electron energy and main electron beam energy.
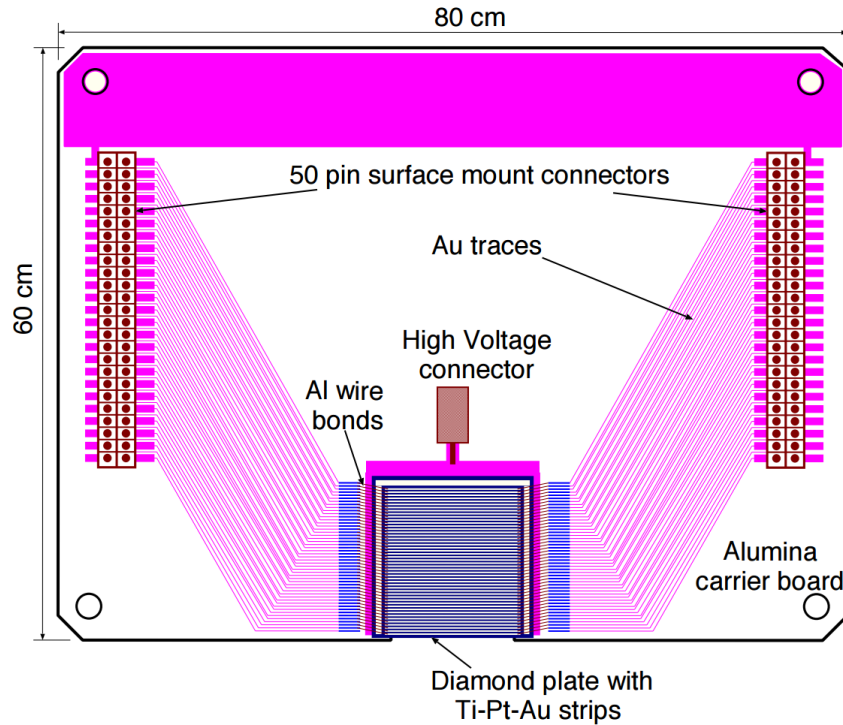
Figure 1-1: Picture of the multi-strip electron detector which is made of vapor deposited diamond.

Parity violating electron scattering experiments such as the QWeak experiment at JLab, which measured the weak mixing angle away from the Z^0 pole, rely heavily on the knowledge of electron beam polarization. The QWeak experiment at JLab demanded a polarimeter which could measure the average electron polarization to 1% precision within an hour [21, 22]. Since Compton scattering is electron-polarization sensitive, it is a good means of measuring electron polarization. The new Hall-C Compton polarimeter achieves 1% precision in measured value of electron polarization in under an hour [6]. The JLab Hall-C polarimeter was installed on the beam line prior to the liquid hydrogen (QWeak) target and consists of 4 - dipole chicane where a photon beam interacts with the electron beam in a Fabry-Pérot cavity as illustrated in FIG. 4-1 [22]. Unlike the Møller polarimeter, the Compton polarimeter is non-
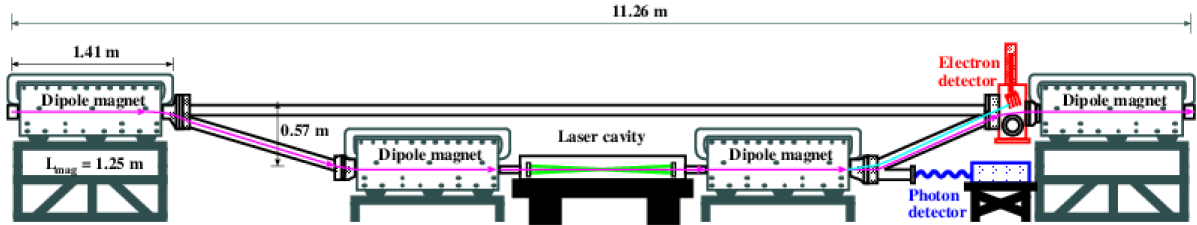
Figure 1-2: Sketch illustrating the 4-dipole (grey boxes) chicane used in JLab Compton Polarimeter along with the photon and electron detectors. The blue line represents the electron beam while the yellow line represents the photon beam.

invasive and continuous since it can be operated simultaneously with a scattering experiment.

Compton polarimeters use a a well known technique of measuring electron beam polarization using Compton scattering with known photon polarization [23, 24, 25, 26, 27, 28, 29, 30]. The Compton scattered electrons and photons can be independently analyzed to obtain the electron beam polarization. Usually the photons have been analyzed to obtain electron beam polarization [23, 24, 25, 26, 27, 28, 29], but in recent times many experiments use analysis of scattered electrons to measure the electron beam polarization [31]. The scattered asymmetry increases with the electron beam energy. The QWeak experiment at JLab Hall-C only used 1 GeV electron beam and therefore it was much more challenging to obtain high degree of precision in electron polarimetry given the scattering asymmetry was just about 0.04. The small asymmetry means that a very high luminosity is required at the Compton scattering point. The high luminosity was obtained by locking and storing a 10W, 532nm laser in a Fabry Pérot cavity. This yields a gain of about 200. Here the electron beam crosses the net photon beam at an angle of 1.3^o. Scattered electrons are separated from the main electron beam which is bent by about 10.3^o by dipole-3 in the chicane. The scattered electrons were detected using a multi-strip vapor deposited diamond detector which is illustrated in FIG. 4-2 and the scattered photons were detected in lead glass detector. The electron detector sits about 17mm (but can be moved perpendicular to the main electron beam) from the main electron beam but diamond detectors have been demonstrated to be radiation hard [32, 33]. Each strip builds a cumulative scattered electron count and therefore, over time an asymmetry number can be assigned to each strip 1.1.

Given the electron energy and photon energy, the Compton asymmetry in Eq. (2) can be calculated from theory [11]. Along with the knowledge of Compton asymmetry and polarization of the photons, the electron polarization can thus be measured to a high degree of precision. Here, the number of electrons seen by every strip of the electron detector individually translates to beam polarization. It might be interesting to note that, it is the number of electrons that were detected (by each strip individually) that is finally used to measure the asymmetry and not the final state electron energy or scattering angle. Such Compton polarimeters have been used in JLab and SLAC and they have all fielded multi-strip electron detectors to improve statistics. Usually

the polarization value obtained from each individual strip in the electron detector is averaged over or in some cases only a certain range of strips are selected for the measurement [13]. Surprisingly, even though only number of electrons counted per strip is used for polarization measurement and not the number distribution measured by all the strips on the whole, asymmetry distribution obtained from the number distribution is very sensitive to the value of speed of light [7].

1.3   Method

1.3.1   Determination of refractive index of free space

Usually the variation in speed of light is studied as a variation in the refractive index of vacuum. If the speed of light was constant w.r.t to a varying parameter, such as photon energy, the refractive index of vacuum is normalized to 1. For Compton scattering of electrons with initial energy ϵ_0 and mass m_e, on photons with initial and final energy and angle ω_0, θ_0 and ω, θ respectively, the Compton scattering cross section and longitudinal asymmetry are given by [8]:

$$\frac{d\sigma}{d\rho} = 2\pi r_e^2 a \left[\frac{\rho^2(1-a)^2}{1-\rho(1-a)} + 1 + \left(\frac{1-\rho(1+a)}{1-\rho(1-a)} \right)^2 \right] \tag{1.3}$$

$$A_l(\rho) = \frac{2\pi r_e^2 a}{d\sigma/d\rho}(1-\rho(1+a)) \left[1 - \frac{1}{(1-\rho(1-a))^2} \right] \tag{1.4}$$

Where $r_e = \alpha\hbar c/m_e c^2 = 2.817 \times 10^{-15}$ m, is the classical electron radius, $\rho = \omega/\omega_{max}$ is the scattered photon energy normalized to its maximum value, and $a = 1/1 + 4\omega_0\epsilon_0/m_e^2$ is a kinematic parameter. As demonstrated in Ref. [7], Compton scattering is very sensitive to tiny deviations of the refractive index from unity due to an amplification of the effect by the square of the initial Lorentz boost (γ_0). For photons scattering off ultra-relativistic electrons in vacuum with $n \approx 1$ (up to $\mathcal{O}[(n-1)^2]$), energy-momentum conservation gives [9];

$$\epsilon_0 x - \omega(1 + x + \gamma_0^2\theta^2) + 2\omega_0(1 - \frac{\omega}{\epsilon_0})\gamma_0^2(n-1) = 0, \tag{1.5}$$

where $x = 4\gamma_0\omega_0 \sin^2\left(\frac{\theta_0^2}{2}\right)/m_e$. The energy-momentum conservation equation (Eq. 1.5) can be re-written as;

$$\omega(n) = \frac{\epsilon_0 x}{1 + x + \gamma_0^2\theta^2} \left(1 + \frac{2\gamma_0^2(n(\omega) - 1)(1 + \gamma_0^2\theta^2)}{(1 + x + \gamma_0^2\theta^2)^2} \right) \tag{1.6}$$

and the maximum energy of the scattered photon which occurs for $\theta = 0$ (called the Compton edge) is given by

$$\omega_{max}(n) = \frac{\epsilon_0 x}{1 + x} \left(1 + \frac{2\gamma_0^2(n(\omega_{max}) - 1)}{(1 + x)^2} \right) \tag{1.7}$$

In the Compton polarimeter, the scattered electrons are momentum analyzed by dipole-3 (see Fig. 4-1) and detected on a position sensitive detector which measures the deflection of the scattered electrons with respect to the unscattered electrons. The deflection of the electron can be calulated from the geometry and operating parameters of the dipole magnet. The vertical deflection for an electron incident on the i-th strip of the micro-strip detector is given by,

$$
\begin{aligned}
\Delta x_i &= [R_i(1 - \cos(\theta_i)) + z_i \tan(\theta_i)] \\
&\quad - [R_0(1 - \cos(\theta_0)) + z_0 \tan(\theta_0)]
\end{aligned} \tag{1.8}
$$

where R_i, θ_i, z_i and R_0, θ_0, z_0 are the bend radius, bend angle and drift distance from the exit of the dipole to the detector plane, for the electrons incident on the i-th strip and the unscattered electron respectively. The bend radius of the unscattered electrons $R_0 = \frac{p_0}{eB} = \frac{L}{\sin(\theta_0)}$, where p_0 is the momentum of the electron beam, B is the magnitude of the dipole field and L is the length of the dipole. The bend radius of the scattered electrons incident on the i-th strip is given by $R_i = R_0 \left(\frac{p_i}{p_0} \right)$. Since the detector is inclined at an angle θ_{det} with respect to the vertical direction the deflection of an electron incident on the i-th strip along the detector plane is given by,

$$
\Delta x_i^{det} = \frac{\Delta x_i \cos(\theta_0)}{\cos(\theta_{det} - \theta_0)} \tag{1.9}
$$

A measurement of the electron deflection is a measurement of the scattered electron momentum, and since the momentum of the scattered electron is related to ρ via momentum conservation by,

$$
p = p_0 + \omega_0 - \rho \omega_{max} \tag{1.10}
$$

the measured electron deflection can be directly mapped to a value of ρ.

The electron detector used in the Hall-C Compton polarimeter has a strip pitch of 0.2 mm, for an electron incident on the i-th strip, its deflection along the detector plane is,

$$
\Delta x_i^{det} = \Delta x_{max}^{det} - 0.2 * (N_{CE} - i), \tag{1.11}
$$

where N_{CE} is the strip number where the Compton edge is located, Δx_{max}^{det} is the deflection of the electrons with minimum momentum, p_{min}, which correspond to the scattered photons with the maximum energy ω_{max}. The maximum deflection Δx_{max}^{det} can be calculated using Eqs. 1.8-1.10 for $\rho = 1$ and similarly by varying ρ between $0 - 1$ in small steps a table of $\rho - \Delta x^{det}$ is built. The $\rho - \Delta x^{det}$ table is fit to a 4-th order polynomial and used to convert the measured Δx_i^{det} for the i-th detector strip to a corresponding ρ_i. This allows the measured longitudinal asymmetry as a function of detector strip-hit to be converted to a measured longitudinal asymmetry as a function of ρ. As mentioned earlier the measured longitudinal asymmetry is related to the calculated asymmetry (Eq. 1.4) according to Eq. 1.1. The measured asymmetry is fit to the calculated asymmetry (Eq. 1.4) with 2 free parameters, the $P_e P_\gamma$ the product of the electron and laser polarizations and N_{CE} the strip location of

the Compton edge. The measured location of the Compton edge is then converted to ω_{max}, and using Eq. 1.7 the deviation of the refractive index from $n = 1$ for a photon energy of ω_{max} is calculated.

If the deviation of the refractive index from $n = 1$ is due to the gravitational field at the Earth's surface ($n_{\oplus} = 1 + 1.39 \times 10^{-9}$ [10]), then the n is independent of the scattered photon energy (ω). If the refractive index is independent of ω, the effect of any deviation of the refractive index from unity can be incorporated into the Compton cross section and longitudinal asymmetry by modifying the scattered photon energy normalized to its maximum value, $\rho \rightarrow \rho(n)$ as,

$$\rho(n) = \frac{\omega(n)}{\omega_{max}(n)} = \rho \left[\frac{1 + \frac{2\gamma_0^2(n-1)(1+\gamma_0^2\theta^2)}{(1+x+\gamma_0^2\theta^2)^2}}{1 + \frac{2\gamma_0^2(n-1)}{(1+x)^2}} \right]. \tag{1.12}$$

The above equation can be written up to $\mathcal{O}[(n-1)^2]$ as;

$$\rho(n) = \rho \left[1 + 2\gamma_0^2(n-1)f(x,\theta) \right], \tag{1.13}$$

where the kinematic function $f(x, \theta)$ is given by,

$$f(x, \theta) = \frac{(1+\gamma_0^2\theta^2)(1+x)^2 - (1+x^2+\gamma_0^2\theta^2)^2}{(1+x+\gamma_0^2\theta^2)^2(1+x)^2} \tag{1.14}$$

The longitudinal asymmetry can then be re-written to incorporate the deviation of the refractive index from $n = 1$ by replacing ρ by $\rho(n)$ in Eq. 1.4. The new modified asymmetry is then fit to the measured asymmetry with three parameters; the product of electron beam and laser polarizations, $P_e P_\gamma$, the strip location of the Compton edge, N_{CE} and $2\gamma_0^2(n-1)$. The new parameter $2\gamma_0^2(n-1)$ is used to extract the deviation of the refractive index from unity.

Using the data of asymmetry measured at every channel for the JLab Hall-C Compton polarimeter, one could perform a least squares fit to the expression for asymmetry w.r.t the photon energy derived above in order to obtain values of n. The beam characteristics change over time, and therefore the Compton polarimeter data sets are limited to a fixed period of time to allow changes to be made. On fitting such data sets, a sample of which is illustrated in Fig. 4-3, we obtain a n for each data set. JLab Compton polarimeter ran for approximately 2 years and the extracted values of n is plotted w.r.t to run number (or data set) in FIG. 4-5.

1.3.2 Determination of limits on SME parameters

Minimal Standard Model Extension (MSME) provides a number of ways to allow Lorentz and thus CPT violation [35]. The leading MSME coefficient which causes direction and polarization dependent speed of light is k_F [36]. In this sub section, we will try to impose limits on the $\tilde{\kappa}_{0+}$ components of κ_F, which is a 3×3 antisymmetric matrix. Using MSME, the dispersion relation for photon in terms of $\vec{\kappa}$ as;
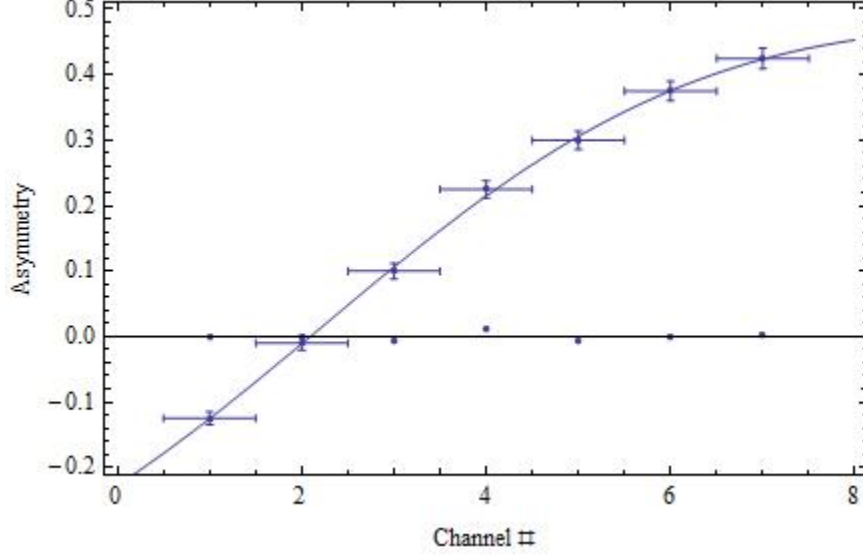
Figure 1-3: Plot showing a sample fit to Eq. (1.4) using data from a single strip read out from SLD Compton polarimeter.

$$\omega = (1 - \vec{\kappa}.\hat{K})K + \mathcal{O}(\kappa^2) \tag{1.15}$$

$$\vec{\kappa} = \left\langle \left(\tilde{\kappa}_{0+}^{23}\right), \left(\tilde{\kappa}_{0+}^{31}\right), \left(\tilde{\kappa}_{0+}^{12}\right) \right\rangle = \langle \kappa_X, \kappa_Y, \kappa_Z \rangle \tag{1.16}$$

where ω is the energy of the photon, $\vec{K}$ is the 3-momentum of the photon. Eq. 1.16 implies that the refractive index of free space is a function of $\vec{\kappa}$. Here Z-direction is parallel to the axes of rotation of the Earth. Using energy conservation in Compton scattering and Eq. 1.16, one could write the index of refraction of free space as;

$$n \approx \left(1 + \frac{2\gamma^2}{\left(1 + 4\gamma\frac{K}{m_e}\right)^2}\vec{\kappa}.\hat{p}\right)$$

$$n - 1 \approx 8.25 \times 10^6 \sqrt{\kappa_X^2 + \kappa_Y^2}\,sin(\Omega t) \tag{1.17}$$

where $\hat{p}(t)$ is unit vector along the 3-momentum of electron beam which for QWeak was $\langle 0.13cos(\Omega t), 0.87sin(\Omega t), 0.48 \rangle$, $K = 2.32$ eV is the momentum of the photon beam, $|\vec{p}| = \epsilon_0 = 1.165$GeV is the electron beam energy, $\gamma = 2280$ is the Lorentz boost of the electrons and $\Omega = 2\pi/(23h56m)$ is the frequency of rotation of the Earth. Finally Eq. 1.17 can be numerically expressed by disregarding the phase offset.

Furthermore, given that the JLab Compton polarimeter ran for almost 2 years, one could also study the variation of the refractive index of vacuum as a function of sidereal time and compare it to Eq. 1.17. Fig. 1-5 shows a plot of this variation fit to a pure sinusoid wave with a frequency of Ω, amplitude of $(0.3 \times 10^{-10} \pm 0.2 \times 10^{-9})$,
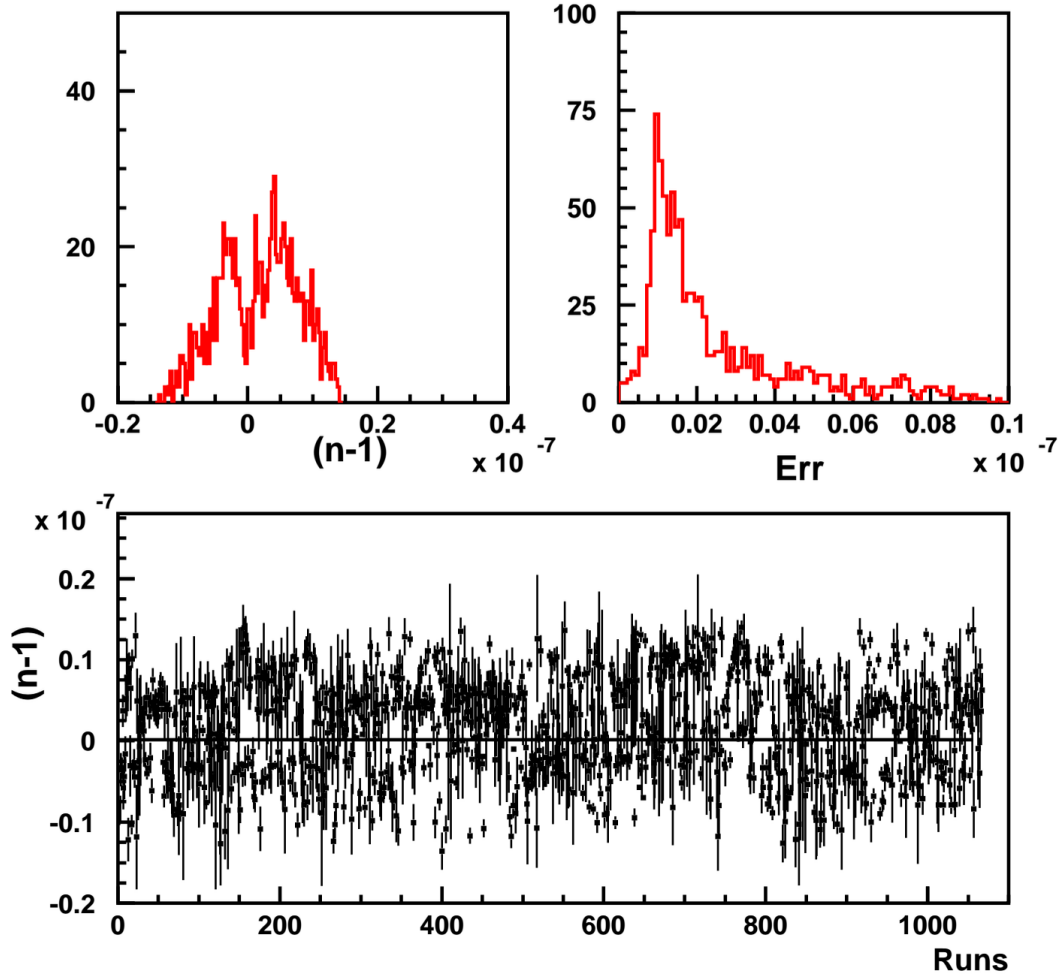
18

Figure 1-4: Plot showing the variation of '$n-1$' as a function of simple time along with accrued errors when fit to a sinusoid.

an offset of $(0.16 \times 10^{-8} \pm 0.02 \times 10^{-8})$, and with $\chi^2 = 1.24$ from 22 d.o.f. With a value of sinusoidal fit amplitude being limited to $< 0.2 \times 10^{-9}$, one could impose a limit on $\sqrt{\kappa_X^2 + \kappa_Y^2} < 2.4 \times 10^{-17}$ from Eq. 1.17.

1.4 Conclusion

Many other tests of CPT symmetry have nevertheless only solidified the case that Lorentz symmetry is indeed held good for a very large range of energy regime. In a dispersive medium whose refractive index is less than one, photons pair produce and in medium whose refractive index is higher than one, charged particles undergo Cherenkov radiation dramatically reducing the maximum energy of these charged particles. Therefore highest energy charged cosmic particles detected and highest energy cosmic photon detected constrains variation of refractive index of vacuum w.r.t photon energy [15]. Cherenkov radiation and pair production are respectively
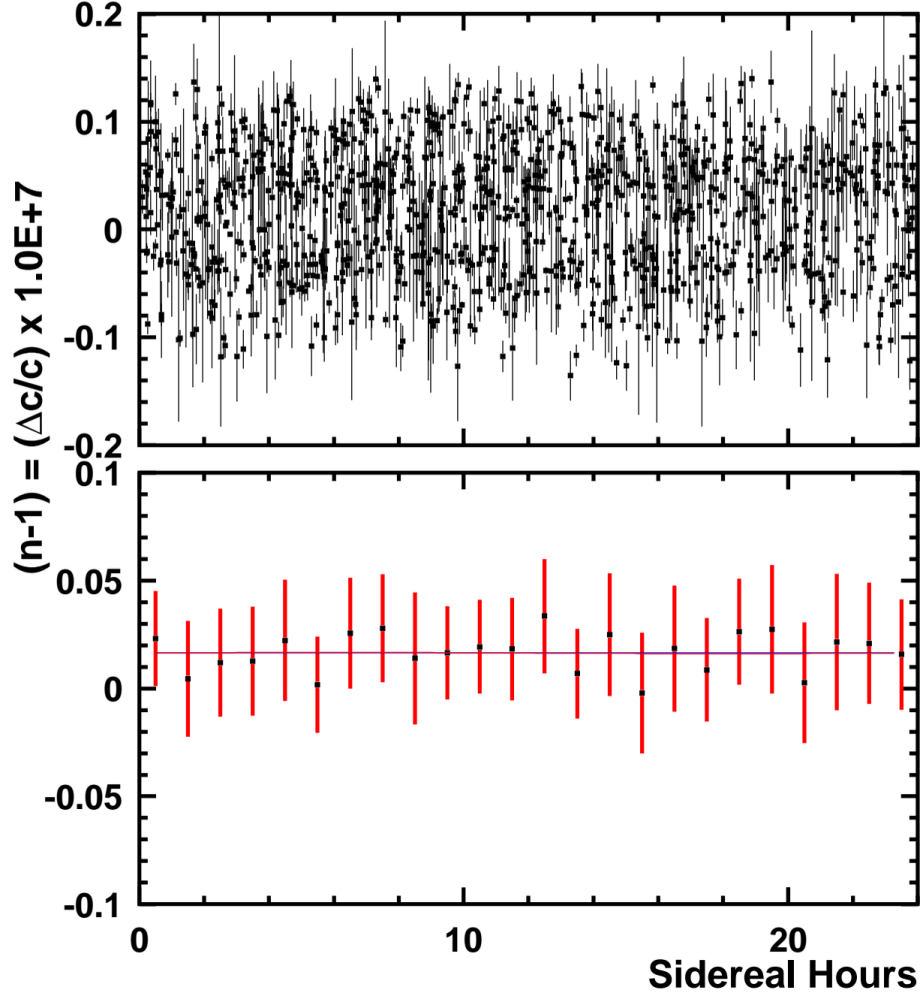
Figure 1-5: Plot showing the variation of '$n - 1$' as a function of sidereal time, with the entire data set from 1200 runs (2 years) rolled into modulo sidereal day.

forbidden if;

$$
\begin{aligned}
|n - 1| \quad &< \quad \frac{m_{p(e)}^2}{2E_{p(e)}^2 - 2\omega_\gamma E_{p(e)} - m_{p(e)}^2} \\
&< \quad \frac{2m_e^2}{\omega_\gamma^2}
\end{aligned}
\tag{1.18}
$$

Along with the values of highest energy cosmic proton observed, which is 10^{22}eV [16], highest energy cosmic electron observed, which is 100 TeV [18], and the highest energy cosmic ray observed, which is 22TeV [17], an experimental exclusion as in Fig. 2-4 could be plotted. Fig. 2-4 uses Eq. 1.18 to arrive at the exclusions for regions named $p \rightarrow p\gamma$, $e \rightarrow e\gamma$ and $\gamma \rightarrow e\bar{e}$ respectively. The exclusion regions named GRB990123 [19] and GRB090423 [20] are obtained from the fact that these gamma
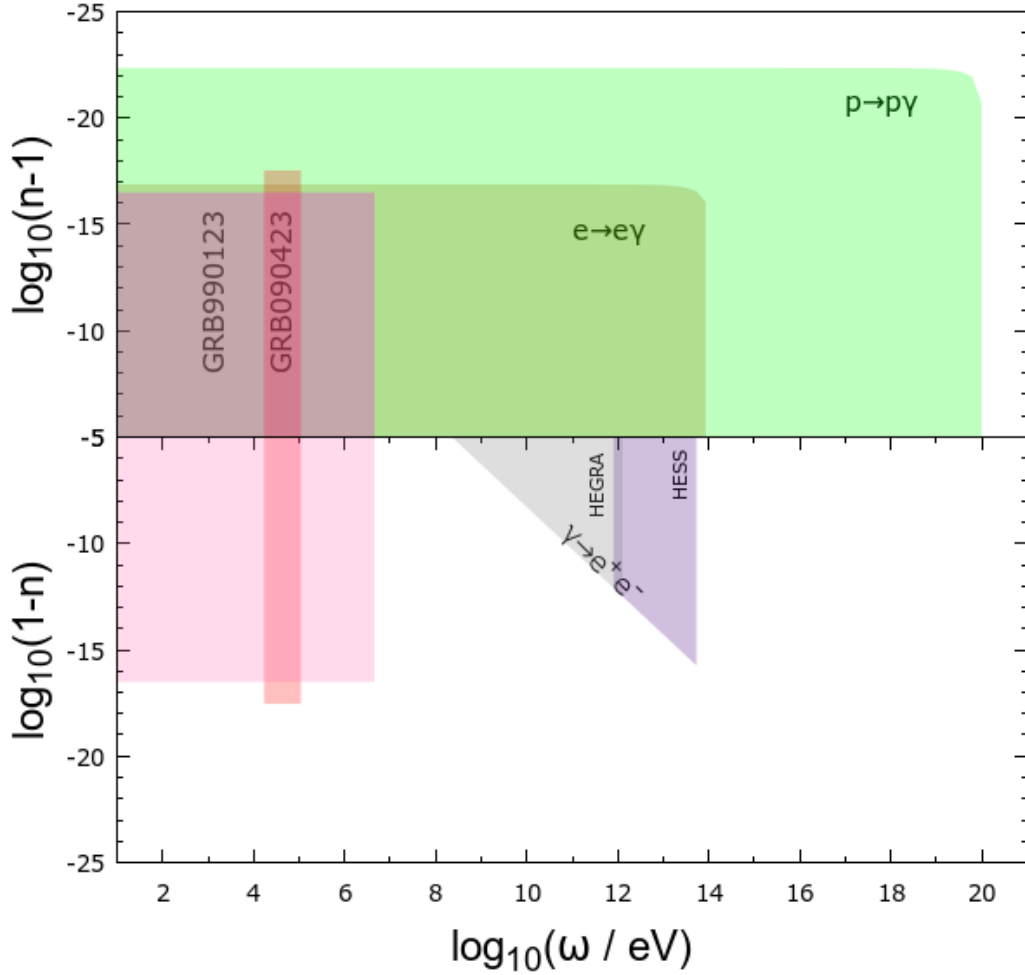
20

Figure 1-6: Plot showing the constraints imposed by various processes on speed of light. Shaded areas are excluded regions.

ray burst occured at a distance of $z = 1.6$ and 8.1 respectively, with a time delay in hard and soft parts of the spectra being 22s and 10.3s. This exclusion follows from the constraint that $|n-1| < \Delta tc/D$, where D is the distance to the gamma ray burst.

On averaging the values of n obtained from the least squares fit to each data set in FIG. 4-5, we obtain a value of $n = 1 + (0.18 \times 10^{-9} \pm 0.02 \times 10^{-9})$. It is important to note that this value for $n = 1 + (0.18 \times 10^{-9} \pm 0.02 \times 10^{-9})$ is not excluded in the plot shown in FIG. 2-4 $((1-n)$ side). A limit of $\sqrt{\kappa_X^2 + \kappa_Y^2} < 2.4 \times 10^{-17}$ also implies that $\sqrt{\left(2c_{TX} - (\tilde{\kappa}_{0+}^{YZ})^2\right)^2 + \left(2c_{TY} - (\tilde{\kappa}_{0+}^{ZX})^2\right)^2} < 2.4 \times 10^{-17}$ [5].

Chapter 2

Mississippi State Axion Search

Abstract

The elegant solutions to the strong Charge-Parity (CP) problem predict the existence of a particle called axion. Thus, the search for Axion like particle (ALP) has been an ongoing endeavor. The possibility that these axion like particles couple to photons in presence of magnetic field gives rise to a technique of detecting these particles known as Light shining through a wall (LSW). MASS is an experiment employing the LSW technique in search for axion like particles. The apparatus consists of two Radio Frequency (RF) cavities, both under the influence of strong magnetic field and separated by a lead wall. While one of the cavities houses a strong RF generator, the other cavity houses the detector systems. The MASS apparatus looks for excesses in RF photons that tunnel through the wall as a signature of candidate axion-like particles. The concept behind the experiment as well as the projected sensitivities are presented here.

2.1   Introduction

The axion was proposed to solve the strong CP problem [37]. Axions have been proposed as a good cold dark matter candidate [38]. In addition to other super-symmetric dark matter candidates, axions are included as dark matter constituents especially in super symmetric extensions of the standard model [39].

A single parameter, the axion decay constant, f_a is sufficient to describe the physics of axions.

$$f_a = 6 \times 10^{-6} eV \frac{10^1 2 GeV}{m_a} \tag{2.1}$$

where m_a is the mass of the axion. Axions and ALPs are characterized by small masses arising from the shift symmetry of the ALP field, $\phi(x)$. The shift symmetry $\phi(x) \rightarrow \phi(x) + const.$ prohibits explicit mass terms ($\propto m_\phi^2 \phi^2$) in the ALP Lagrangian. The only way an ALP field could interact with standard model particles is via derivative couplings ($\propto \partial\phi/f_a$). This significantly suppresses their interactions below the f_a
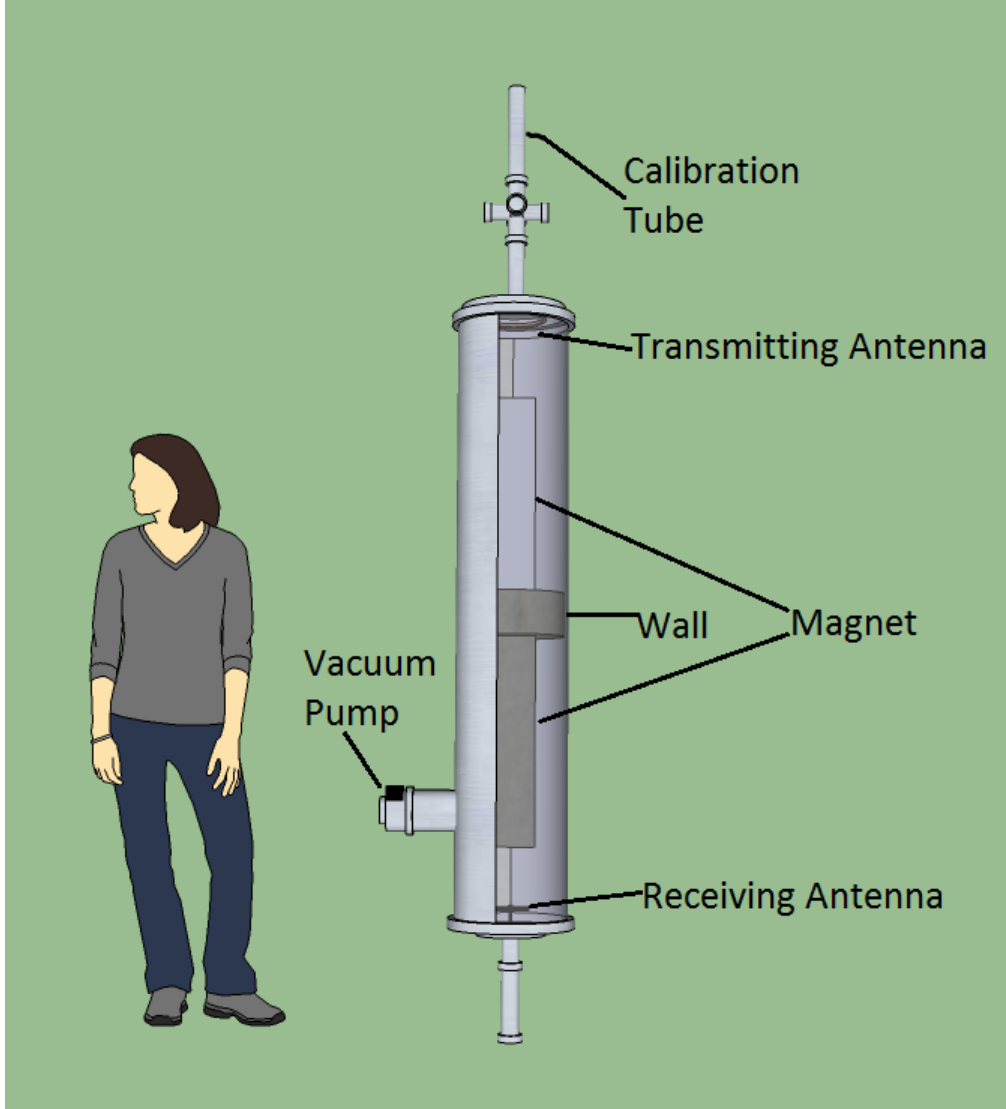
Figure 2-1: Basic schematic diagram of the MASS apparatus.

scale, effectively making ALPs weekly interacting sub-eV particle (WISP) candidates [40]. Furthermore, the two most relevant two photon couplings can be written for both pseudo-scalar and scalar ALPs respectively as;

$$\mathcal{L}_{\phi^{+(-)}\gamma\gamma} = -\frac{g_{+(-)}}{4}F_{\mu\nu}\tilde{F}^{\mu\nu}\phi^{+(-)} \tag{2.2}$$

where, $F_{\mu\nu}$ is the electromagnetic field, $g_{+(-)} = g_\gamma(\alpha/\pi f_a)$, $g_\gamma \approx -0.97$ in Kim-Shifman-Vainshtein-Zacharov (KSVZ) model [41] or $g_\gamma \approx -0.36$ in Dine-Fischler-Srednicki-Zhitnitskii (DFSZ) model [42] , and α is the fine structure constant.
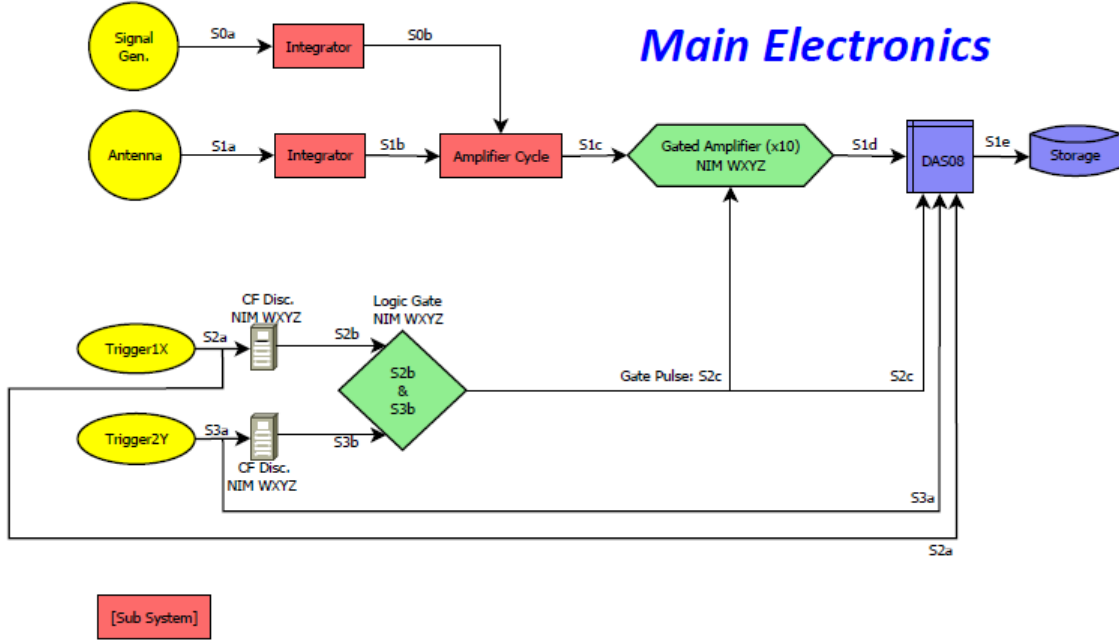
Figure 2-2: Schematic diagram showing the fast electronics in line before the data is written to disk.

2.2 Method

In the MASS experiment, Primakoff effect is employed to put the LSW technique to test where the incident photon couples with the magnetic field to create lightly interacting ALPs which pass through a barrier, regenerating to photons on the dark side of the barrier, while ideally no photons pass through the barrier. The regenerated photons have the same characteristics as the incident photons, *i.e.* they are of the same frequency, phase and couple to the same electromagnetic mode. Since photons are regenerated via an ALP, the rate of regeneration (R) is given by [43];

$$R = N_\gamma \epsilon_c Q_d P_{\gamma \to ALP} P_{ALP \to \gamma} \tag{2.3}$$

$$P_{\gamma \to ALP} = P_{ALP \to \gamma} = \left(\frac{gB}{\frac{m^2}{2\omega}} \right)^2 Sin^2 \left(\frac{m^2 L}{4\omega} \right) \tag{2.4}$$

where N_γ is the number rate of photons, ϵ_c is photon capture efficiency, Q_d is the detector quantum efficiency, $P_{\gamma \to ALP}$ is the probability of conversion of a photon to a scalar ALP, $P_{ALP \to \gamma}$ is the probability of conversion of a scalar ALP to a photon, g is the coupling constant, m is the mass of the ALP, B is the magnetic field strength, ω is the energy of the photons and L is the length of the cavity under magnetic field.

25

2.3 Apparatus

The MASS apparatus consists of two tunable evacuated cavities as shown in Figure 4-1. These two cavities are mutually isolated. The "light" cavity houses a StreakHouse ^{TM} transmission antenna [44], capable of transmitting integral multiples of 410 MHz and the "dark" cavity houses an antenna capable of mapping local field in all three spatial axes. A compact dipole magnet bathes the two cavities in a magnetic field in the radial direction while a solenoid is used to create a magnetic field along the axis of the cavities (Z-direction). The radial magnetic field produced by the dipole magnet was mapped using a Di-Phenyl Picryl Hydrazyl (DPPH) probe and is presented in Figure 4-3. The solenoid is only used to tune the cavity and thereby has a low field strength output (< 0.5 T). The transmission antenna is mounted at the end of a calibration tube, precise to within 1 nm which allows for additional fine tuning of the cavity. The other end of the calibration tube provides for a number of electronic feed thoughts. Feed through for the receiving antenna electronics is completely separated from the feed through for the main transmission antenna.
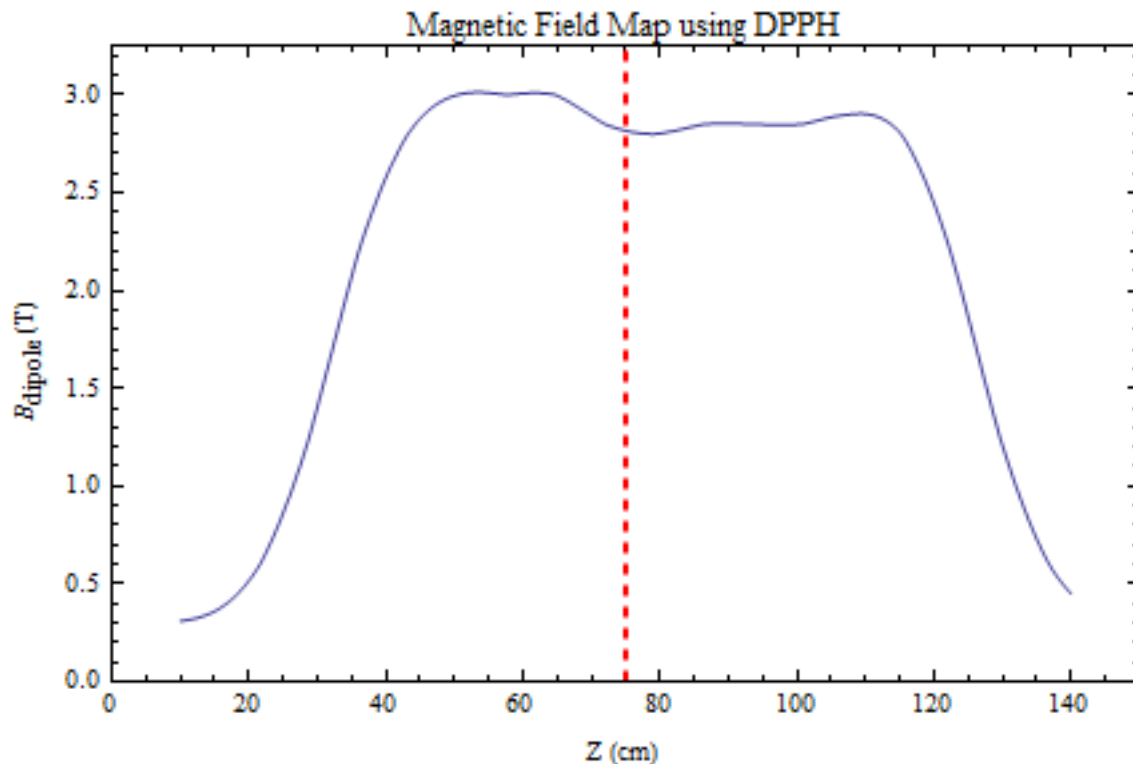

Figure 2-3: Plot showing the dipole magnetic field profile in the 2 cavities used in MASS. On the left hand side of the red line is the "light" cavity and on the right hand side of the red line is the "dark" cavity.

The cavities are usually tuned simultaneously to TM_{010} and TM_{020} where the most fundamental mode corresponds to 410 MHz. About 120 W of RF power is dumped into the "light" cavity through the transmission antenna. The transmission power gives a measure of number rate of photons, N_γ, in Eq. (3). A precise measurement

of the standing wave ratio (SWR) of the receiving antenna gives a measure of the product of photon capture efficiency and its quantum efficiency, $\epsilon_c Q_d$, in Eq. (3).

MASS experiment employs a redundant frequency lock-in technique to control signal to noise ratio in the apparatus. The primary signal is generated using a 16-bit programmable digital oscillator which is then amplified a number of times to reach 120 W of continuous transmission power. Both the receiver signal and the primary signal are rectified, integrated and normalized (hereby referred to as processed) such that their difference is ideally null except in the case of there being a regenerated photon (Figure 4-2). Processing involves continuous rectification which converts all negative components to positive. Furthermore, the rectified signal is integrated over 1 ms before the running integrand is reset to zero. The regenerated photons show up as small excesses in the running integrand at the end of the corresponding 1 ms time period. Integrating the receiver signal also reduces the amount of digitized data by a factor of 410×10^3, since the primary signal is 410 MHz and the integrated signal has a frequency of 1 kHz due to the integration time period being 1 ms. The difference between the processed primary signal and the processed receiver signal has the same frequency and phase information as that of the processed primary signal, therefore the processed primary signal also serves as the reference for the three SR 530 [45] lock-in amplifiers. The difference of the processed receiver signal and the processed primary signal is then subject to three sets of SR 530 lock-in amplifiers which use the processed primary signal as a reference providing a signal to noise ratio better than 10^{18} accounting for residual thermal noise and quantum fluctuations.

The processed and amplified receiver signal is then digitized and written to disk. A set of trigger antenna within the apparatus located around the "dark" cavity pickup on external noises and creates a gate during which time the processed and amplified primary signal is not written to disk.

2.4 Conclusion

Taking into account the inhomogeneity of the magnetic field, the characteristics of the two main antennae, residual RF field on the "dark side of the cavity" and the thermal noise, all of which contribute to the uncertainty in measured rate of regenerated photons, the possible sensitivity of MASS to scalar and pseudo scalar ALPs is calculated using Eq. (3) & (4), as presented in Figure 2-4. It might be important to note that since the exclusions that MASS can provide for scalar and pseudo scalar ALPs are similar to each other, Figure 2-4 has plotted the sensitivities to two different cavity modes, each a multiple of the fundamental frequency of 410 MHz, both of which are accessible in the MASS apparatus.

Even though the sensitivity that MASS can provide in the low mass regime (10 μeV - 100 μeV) for both scalar and pseudo scalar ALPs will only be comparable to the currently available limits, and not any better, it shall demonstrate the feasibility of using the LSW technique with RF photons.

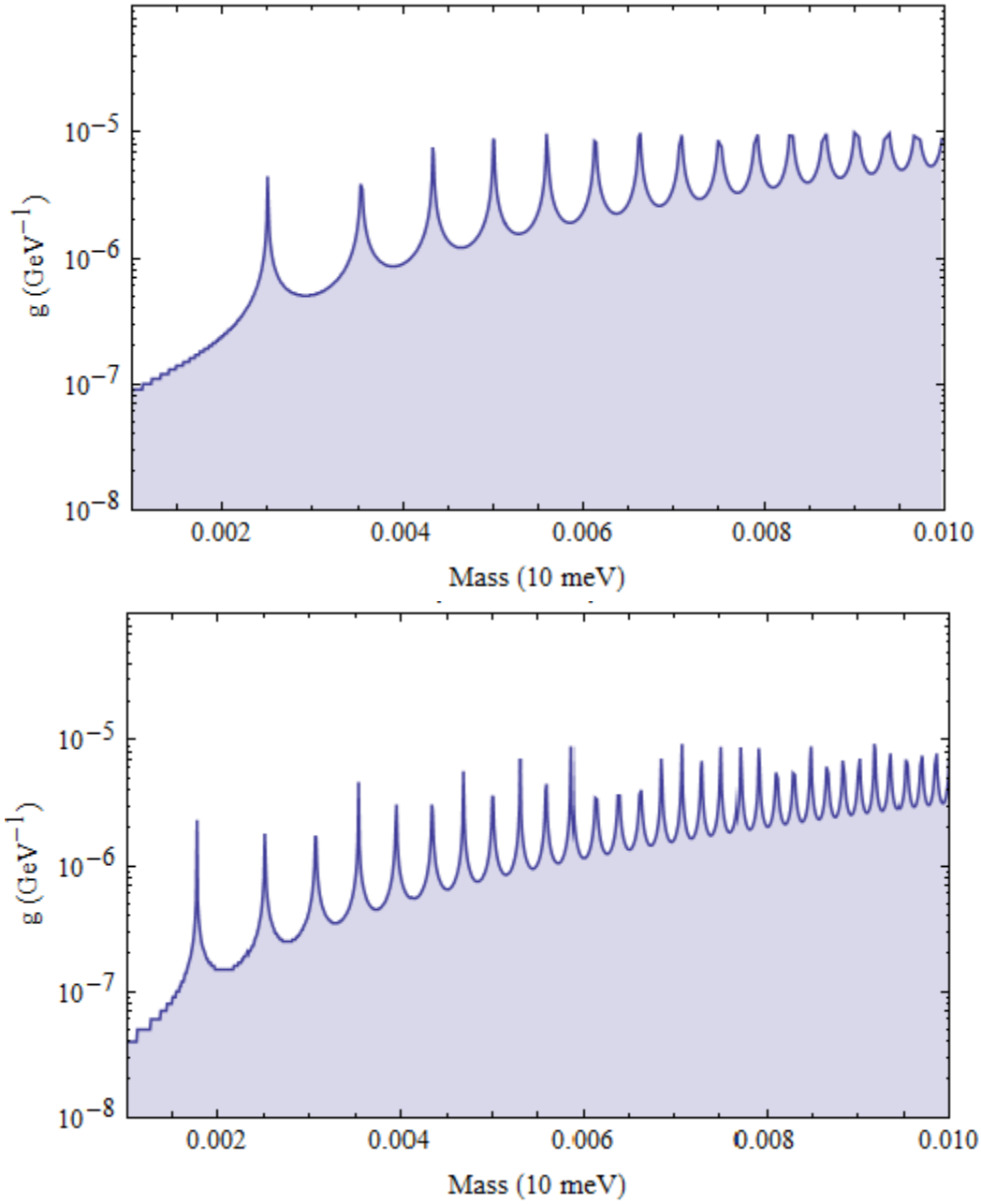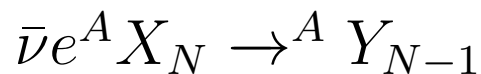Figure 2-4: (Top) Plot showing the sensitivity of MASS to scalar ALPs when the cavities are tuned around 410 MHz with a C.L of 95%. (Bottom) Plot showing the sensitivity of MASS to pseudo-scalar ALPs when the cavities are tuned around 820 MHz with a C.L of 95%.

Chapter 3

Detecting the Solar Anti-Neutrino Flux Using Enhanced Crystal Resonance

$$\bar{\nu}e^{A}X_{N} \rightarrow^{A} Y_{N-1}$$

Abstract

We explore the possibility of detecting the thermal flux of low-energy antineutrinos arising from neutrino pair processes taking place in the solar core. We make use of two techniques in order to attain reasonable detection rates in a modest detector: (a) neutrino capture on electron capture and beta decaying nuclei and (b) resonant enhancement due to crystal lattice scattering. Exploiting the fact that the natural crystal spacing of both ^{163}Ho and ^{187}Os coincides very closely with the resonance energy for neutrino capture and that the cross-section depends on the neutrino flux density, we expect the event rate to scale quadratically with the target mass. We present estimates for the expected rates on these two targets and outline the requirements for experimental detection. If realized, such an experiment would stand as the smallest solar neutrino detector ever constructed.

3.1   Introduction

Considerable effort has taken place over the past sev eral decades in predicting and measuring the flux of solar neutrinos. Measurements of such processes not only helped solidify the solar fusion mechanism, but also helped first reveal and later confrm the phenomenon of neutrino oscillations. To date, most of such measurements have relied on the detection of neutrinos produced from nuclear mechanisms (^{8}B, ^{7}Be, etc.). This chapter focuses on the possible detection of neutrinos created in the solar core via an alternative production mechanism: leptonic production of neutrinos from the sun. The flux of both neutrinos and anti-neutrinos was originally calculated by Haxton

and Win and could represent a novel window into the sun's core temperature. We concentrate on the anti-neutrino flux for this chapter. Several mechanisms contribute to the anti-neutrino flux, but as they are mainly dominated by Compton and plasmon processes, they readily avoid a strong dependence on nuclear cross-sections or form factors. Their extremely high flux density per flavor (of order $10^8 - 10^9 \bar{\nu}_e/cm^2/s$) makes seeking detection tempting. However, their relatively low average energy (2 keV) also makes detection challenging from an experimental perspective. In this chapter, we take advantage of several factors that, although in isolation are insufficient to allow feasible detection, happily conspire to allow detection within a very modest-scale experiment. By making use of neutrino resonant capture on a crystal target, it is possible to take advantage of (1) a detection channel that depends on neutrino flux density, rather than neutrino flux, and (2) crystal lattice enhancement to provide a viable mechanism for detection. Only a few selected target isotopes are amenable for such use. However, as will be shown, such targets are perfectly suited for measuring the solar anti-neutrino flux with sufficiently high statistics.
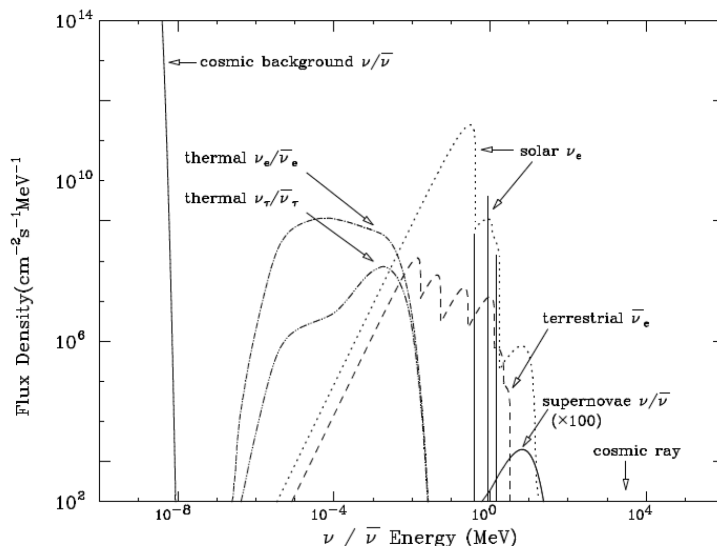

Figure 3-1: Natural neutrino sources. The terrestrial $\bar{\nu}_e$ flux and continuous flux of extragalactic supernova neutrinos of all flavors are from Krauss et al, while the solar (fusion) $\bar{\nu}_e$ flux is the standard solar result of Bahcall et al. The solar $\bar{\nu}_e$ flux is from Haxton and Lin.

3.2   Proposed Detection Scheme

In order to ascertain the feasibility of detecting these solar anti-neutrinos using crystals, we need to first iso late a process that even allows such an interaction to take place. The requirements on such a process are quite stringent: the anti-neutrino flux peaks at 2 keV and falls exponentially to essentially zero by about 20 keV, leaving only a narrow energy window to operate. Most neutrino reactions have thresholds

well-above this energy range and are thus not suitable. Although coherent and electron scattering are of course possible, the imparted energy used for triggering is often too low to provide a reasonable detection scheme. Instead, we turn to a resonance process as a more viable though yet untested scheme for detection.

Consider the process of ordinary electron capture (β-decay), whereby an electron (anti) neutrino is spontaneously created:

$$(A, Z) + e^- \rightarrow (A, Z - 1) + \nu_e \tag{3.1}$$

and

$$(A, Z - 1) \rightarrow (A, Z) + \bar{\nu}_e + e^- \tag{3.2}$$

The above reactions opens the following channels for detection of anti-neutrinos:

$$(A, Z) + e^- + \bar{\nu}_e \rightarrow (A, Z - 1) \tag{3.3}$$

Reaction 3 can be considered the reserve process of β-decay. Because the reaction combines three different targets into one, the reaction is resonant in nature. Depending on the target material used, the cross-section can be compared against either the parent electron capture process or the β-decay process, as the matrix elements are common to both.

Reaction 3 has been previously explored within the context of reactor neutrinos, geo-neutrinos, and even relic neutrinos. Here, we explore the reaction within the context of detecting solar anti-neutrinos. In the analog case of electron capture, the decay produces a mono-energetic neutrino and (typically) an excited nucleus which emits a photon. In neutrino resonance capture, the reaction takes place only for specific neutrino energies which sat isfy the condition $E_\nu = Q + E_\gamma$, where E_γ is the incoming neutrino energy, E is the de-excitation photon, and Q is the parent-progeny mass difference. Note that Q in this case can be positive or negative; the former making the mirror decay electron decay, while the latter corresponding to β-decay. As the energy of our solar neutrinos does not exceed more than 20 keV, the number of targets that can undergo this transformation is severely limited (their Q value must also be correspondingly small). As a result, we concentrate on just two isotopes for this process: ^{163}Ho and ^{187}Os.

In the case of 163Ho, we are mainly interested in the electron capture process:

$$^{163}Ho + e^- + \bar{\nu}_e \rightarrow^{163} Dy^* \rightarrow^{163} Dy + \gamma \tag{3.4}$$

With a Q value of just 2.555 keV, the electron capture process can only engage a few of the low energy electron shells (typically the M and N shells). However, the L shell electron configuration for dysprosium sits only about 6 keV above the Q-value. Therefore, a neutrino with sufficient energy to overcome that gap has the potential to engage in the resonance process. The corresponding 8-9 keV mono-energetic photon emitted in the process provides an excellent x-ray signature of the reaction.

Likewise, ^{187}Os also provides a potential channel for anti-neutrino detection:

$$^{187}Os + e^- + \bar{\nu}_e \rightarrow^{187} Re^* \rightarrow^{187} Re + \gamma \tag{3.5}$$
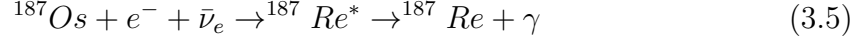
Unlike ^{163}Ho, ^{187}Os is a stable isotope, since the mass difference between parent and progeny is negative (Q = 2469 keV). Again, if an incoming neutrino has sufficient energy to reach any of the electron configuration shells, it will be subject to a resonance transition and emit a mono-energetic X-ray in the de-excitation process. Several shells near 12 and 2 keV are of potential interest within our context of solar anti-neutrinos. For a more complete list of relevant properties of osmium and holmium, see Table 1.

In both cases, the signature for either reaction 5 or 4 are x-rays. Fortunately, both ^{163}Ho and ^{187}Re (the mirror isotope to ^{187}Os) have been the subject of recent interest in neutrino physics, specifically for direct neutrino mass measurements. As a result, a great deal of detector development is underway for using such target materials in various bolometric calorimeters. Experiments such as MARE, ECHO, and HOLMES are recent examples of such experiments. Using such materials embedded in X-ray detectors is fairly well-advanced, with energy resolutions of better than 10 eV already achieved.

In order to estimate the (non-coherent) cross-section of the above reactions, it is useful to use either the equivalent electron capture or beta decay lifetime as a bench mark for the relevant matrix element. For this chapter, we use the procedure outlined by Cocco, Mangano, and Messina. For electron capture, the total decay rate can be written compactly as the following (we use the convention $h/\pi = c = 1$):

$$\Gamma_{EC} = \frac{ln2}{t_{1/2}} = \frac{G_\beta^2}{2\pi^3}\Sigma_x n_x C_{x,n}^\nu f_x \tag{3.6}$$

where G_β is the Fermi weak coupling constant, n_x is the occupancy number of a given electron shell x ($n_x = 1$ for filled shells), $C_{x,n}^\nu$ is a shape factor for a given transition with angular momentum change $n = \Delta J - 1$, and f_x is defined as;

$$f_x = \frac{\pi}{2}q_x^2\beta_x^2 B_x \tag{3.7}$$

where $q_x = (Q - E_\nu/m_e$ is the outgoing neutrino energy, β_x is the Coulomb amplitude of the bound-state electron radial wave-function and B_x is the correction due to the overlap between radial wave functions. As the overlap correction is typically small, we do not consider it for our calculations.

It is possible to relate the observed electron capture decay directly to the equivalent cross-section for reaction 4. The reaction is further simplified by the fact that it is also an allowed transition, which renders the correction factor essentially constant. Thus, for a given reaction to a specific electron shell i, the cross-section can be written as:

$$(\sigma\nu)_i = \frac{G_\beta^2}{\pi}n_i C_{i,n}^\nu g_i \rho_i(E_\nu) \tag{3.8}$$

where $\rho_i(E_\nu$ represents the density of states available (here modeled as a Breit-Wigner

Property	Holmium		Osmium	
Relevant isotope	^{163}Ho		^{187}Os	
Progeny	^{163}Dy		^{187}Re	
Transition	$\frac{7}{2}^- \to \frac{5}{2}^-$		$\frac{1}{2}^- \to \frac{5}{2}^+$	
Q-value	+ 2555 eV		-2469 eV	
Natural abundance	N/A		1.56%	
Half-life	4570 y		stable (41.2 Gy)	
Binding energies				
K-Shell	53789 eV		71676 eV	
L-Shell	9046 eV	8581 eV	12527 eV	11959 eV
M-Shell	2047 eV	1842 eV	2932 eV	2682 eV
N-Shell	414.2 eV	333.5 eV	625.4 eV	518.7 eV

Table 3.1: Relevant particle properties of osmium and holmium evaluated for this study. For the binding energies, just the s and $p_{1/2}$ states are shown. For ^{187}Os, we also list the half-life of it's parent isotope, ^{187}Re.

distribution with a central value of $E_\nu + Q - E^i_\gamma$) and,

$$g_i = \frac{\pi}{2}\beta_i^2 B_i \tag{3.9}$$

By combining the above expressions, we can re-write the cross-section as:

$$(\sigma\nu)_i = \frac{2\pi^2}{q_i^2}\frac{ln2}{t_{1/2}}z_i\rho_i(E_\nu) \tag{3.10}$$

where zi is the occupancy-weighted ratio of the Coulomb amplitude of the bound-state electron radial wave function with respect to the total sum available to the electron capture rate:

$$z_i = \frac{n_i C^\nu_{i,n} f_i}{\Sigma_x n_x C^\nu_{x,n} f_x} \tag{3.11}$$

In this form, one essentially removes almost all dependence on the matrix element and the cross-section is entirely determined by measurable quantities. Since reaction 4 is an allowed transition, the overlap function $C^\nu_{i,0}$ is essentially a constant and can be removed from the sum.

The case for reaction 5 is a bit trickier because the mirror process is not an electron capture process but rather β-decay, and it is further complicated by the fact that it is a first unique forbidden transition. If we limit our cross-section evaluation simply to s-shell captures, then for n-forbidden decays, the correction factor z_ν can be written more generally as;

$$C^\beta_n(p_e, p_\nu) = |^A F^{(0)}_{n+1,n+1}|^2 \frac{R^{2n}}{((2n+1)!!)^2}u_n(p_e, p_\nu) \tag{3.12}$$

where f^β_n is the integral of the Fermi function of the beta decay process and $u_n(p_e, p_\nu)$ are functions of the neutrino and electron momenta from the reaction. Note that if

$\Delta J = 1$ and $f_n^\beta = \Sigma n_x C_x f_x$, then one reproduces Eq. 10. Once again, much of the matrix dependence is essentially removed from consideration, since it can be linked directly to a well-measured decay rate in a similar channel.

From the above, one can therefore estimate the rate for each target. Because the cross-section depends on the density of states of the incoming neutrino, and because the reaction is resonant, the rate is actually proportional to the flux density rather than the flux. If we define the number of neutrinos per unit volume as n_ν and the number of target nuclei as n_T , then the total observed rate (R) is given by:

$$n_\nu = \int \frac{1}{\nu} \frac{d\Phi}{dE_\nu} dE_\nu \tag{3.13}$$

$$R = \int n_T \frac{d\Phi}{dE_\nu} \frac{e\pi^2}{q_\nu^2} \frac{ln2}{ft_{1/2}} \rho(E_\nu) dE_\nu \tag{3.14}$$

where $d\Phi/dE_\nu$ is the neutrino flux per unit energy.

Cross-section values for the holmium and osmium targets hover near $10^{-49} cm^2/MeV/s$ and $10^{-57} cm^2/MeV/s$ respectively. Although these targets have been the subject of interest in the past, particularly for geo-neutrino and reactor neutrino detectors, the practical considerations required to make a feasible measurement are too large to overcome. The holmium reaction involves a radioactive isotope, where only mCi of activity have been achieved. The osmium target is attractive from the vantage point that it is stable, but it is one of the most precious metals in the market. In both cases the signature of the reaction is an x-ray of several keV thus requiring that the target needs to be extremely thin or act as the detector itself; both diffcult to realize for very large masses. Therefore, one needs to consider some other mechanism if one hopes to make detection of such low energy neutrinos feasible.

Such hope comes from the realization that the resonant neutrino momentum needed to activate these reactions is of the same scale as the natural lattice spacing of these materials. Should the incoming neutrino momentum coincide exactly with the lattice spacing, the reaction rate should scale at the square of the number of lattice sites, rather than linearly. Such coherent enhancement of the cross-section would mimic what is readily used in x-ray measurements. We discuss the possibility of using such a coherent enhancement mechanism in the next section.

3.3 Crystal Enhancement

For this argument, we borrow the approach and formalism typically adopted in soft x-ray spectroscopy. Let us consider the incoming neutrino as being reasonably described as a plane wave whose satisfies the Dirac equation, $\phi_a(k_\mu, x_\mu) = d(k_\nu e^{ik_\mu x^\mu}$. Now, consider the case where the target nuclei are arranged along a regular lattice whose sites locations correspond to the positions $\vec{r}_n + \vec{R}_m$ (r_m indicates positions within a given lattice, while $\vec{R}m$ indicates individual lattices). If this is the case, then it is possible to separate the enhancement due to the lattice and that due to individual

nuclear sites, upon which the amplitude of any transition can be written as:

$$\phi \propto |\Sigma_{n,m} f_n(\rho_\nu) e^{i\vec{Q}.(\vec{R}_m + \vec{r}_m)}|^2 \tag{3.15}$$

$$\phi \propto |\Sigma_n f_n(\rho_\nu) e^{i\vec{Q}.\vec{r}_n)}|^2 \times |\Sigma_m e^{1\vec{Q}.\vec{R}_m}|^2 \tag{3.16}$$

$$\phi \propto |F(\rho_\nu|^2 \times |L(\vec{Q})|^2 \tag{3.17}$$

Here, $F(\rho_\nu$ is the structure factor of the unit cell, and depends only on the different sites within the unite cell; while $L(\vec{Q})$ is the lattice structure function, and it encapsulates the information (and enhancement) of the lattice itself. Note that since the interaction is weak rather than electromagnetic, the form factor $f_n(\rho_\nu)$ would essentially be replaced by the wave function considered in the previous section.
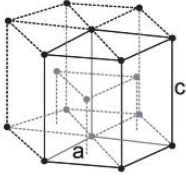
For a regular lattice defined by the points $\vec{R}_m$, there exists a set of reciprocal vectors, $\vec{G}$ such that $e^{1\vec{G}.\vec{R}_m} = 1$. In which case, in the limit that the number of lattice sites becomes very large, then:

$$L(\vec{Q} \to \Sigma\delta^3(\vec{Q} - \vec{G}) \tag{3.18}$$

and hence the transition probability scales as the square of the number of targets. The vector $\vec{Q}$ in this case represents the 3-momentum transfer imparted on the lattice during an interaction.

The exploration of using crystals for neutrino scattering is nothing new and was most originally explored by Weber. Several authors have challenged the scaling of the cross-section in this manner. Indeed, most of the cases considered involve coherent neutrino scattering, where the final states include an outgoing neutrino with modified momentum p'_ν. When one integrates over all possible states, forward scattering dominates and, on average, the phase-space scales as $1/N$ and the cross-section's linear dependence is restored. However, in the channel we have chosen to study, the reaction is already resonant, meaning the phase space is essentially singular. Hence, there is no integration over all states as only one state is truly available. As long as the reciprocal vector $\vec{G}$ and the resonance condition coincide, the scaling remains truly quadratic in the number of targets. In this manner, such scattering is more analogous to superradiance than Bragg scattering, i.e. the enhancement stems from the crystal acting as a coherent object to decay into one final state. The remaining challenge, then, is to determine whether the crystal structure of the targets we have explored do indeed conspire to allow such a decay channel to become available. Both holmium and osmium possess a hexagonal close packed (hcp) lattice structure, with two lattice spacings being identical (a = b) and the third at an ideal fixed ratio c/a of 1.633. The specific measured quantities for each target considered are summarized in Table 2. From these two quantities, it is possible to construct the basis functions for in both cartesian and reciprocal space:

35

TABLE II. Relevant lattice properties of osmium and holmium targets used for this study.

Property	Holmium	Osmium
Crystal structure	Hexagonal close packed	
Lattice constants	(3.58 Å, 3.58 Å, 5.62 Å)	(2.73 Å, 2.73 Å, 4.32 Å)
c/a ratio	1.570	1.582
Lattice Volume	62.24 Å^3	27.995 Å^3
Density	8.795 g/cm^3	22.59 g/cm^3
Debye Temperature (Θ_D)	190 K	487 K

$$\hat{g}_1 = (\frac{4\pi}{a\sqrt{3}}, 0, 0); \quad \hat{t}_1 = (\frac{a\sqrt{3}}{2}, -\frac{a}{2}, 0) \tag{17}$$

$$\hat{g}_2 = (\frac{2\pi}{a\sqrt{3}}, 1, 0); \quad \hat{t}_2 = (0, a, 0) \tag{18}$$

$$\hat{g}_3 = (0, 0, \frac{2\pi}{c}); \quad \hat{t}_3 = (0, 0, c) \tag{19}$$

$$\tag{20}$$

$$\vec{\mathbf{G}} \equiv \vec{G}_{hkl} = h\hat{g}_1 + k\hat{g}_2 + l\hat{g}_3 \tag{21}$$

$$\tag{22}$$

For a hcp lattice, each cell consists of two atoms (located at the center and $\vec{n} = \frac{2}{3}\hat{t}_1 + \frac{1}{3}\hat{t}_2 + \frac{1}{2}\hat{t}_3$ positions). From the above information, one can therefore determine both equivalent momenta that correspond to the lattice spacing as well as its corresponding structure function:

$$|F_{hkl}|^2 = \frac{M_{hkl}}{2}|1 + e^{i\vec{n}\cdot\vec{G}_{hkl}}|^2 \tag{23}$$

The integers h, k, l are the reciprocal index components of the vector $\vec{\mathbf{G}}$ and each index represents a family of planes which can be generated by reflection or rotation by $\frac{\pi}{2}$. The multiplicity factor M_{hkl} accounts for the fact that certain reflection planes can contain more than one lattice vector. To be slightly more complete, we also include the Debye-Waller factor, which accounts for the thermal vibrations in the crystal. In general, the Debye-Waller factor is geometry dependent; however, for simplicity we assume for this calculation a cubic lattice configuration; upon which the broadening due to thermal effects can be approximated by the function

$$|D_F|^2 = e^{-\frac{\epsilon_d|\vec{\mathbf{G}}|^2}{2}}, \tag{24}$$

$$\epsilon_d = \frac{12}{m_u k_b T \mu_D^2}[\Phi(\mu_D) + \frac{\mu_D}{4}], \tag{25}$$

$$\Phi(y) = \frac{1}{y}\int_0^y \frac{z\,dz}{e^z - 1}, \tag{26}$$

$$\text{and} \quad \mu_D = \frac{\Theta_D}{T} \tag{27}$$

Here, m_u is the atomic mass of the target, k_b is the Boltzmann constant, T is the crystal temperature and Θ_D is the Debye temperature of the crystal. As we will discuss below, most of the detectors envisioned for this measurement operate at milliKelvin temperatures, so the suppression due to the Debye-Waller factor is only a small correction to the overall amplitude.

Thus, for given neutrino with incoming momentum p_ν, the total enhancement due to its coherent scattering against the crystal lattice with n_T lattice cells is given by:

$$|L(\vec{\mathbf{Q}})|^2 = n_T^2 \frac{M_{hkl}}{2}|F_{hkl}|^2 |D_F|^2 |\frac{1}{n_T}\sum_{n_T}\delta^3(\vec{p}_\nu - \vec{\mathbf{G}})|^2 \tag{28}$$

If the neutrino momentum happens to match one of the reflection planes for the crystal, the cross-section will scale quadratically with the number of targets, rather than linearly. The challenge is therefore to determine how well the resonances of the reaction coincide with the lattice spacings of the crystal. A minimization search is performed to determine the closest match between the momentum lattice of the crystal and that of the resonances. Results are shown in Table III. For holmium, the $(1, 0, 2)$ crystal orientation falls naturally only 67 eV away from the capture resonance, while for osmium both the $(2, 1, 2)$ and $(1, 0, 0)$ orientations are within 100 eV of

the main resonance. The osmium $(2, 1, 2)$ is particularly attractive, since it is only 0.14 eV away from the capture resonance, but this selects neutrinos with very high energy (15 keV), so at the very end of the tail of the solar flux distribution.

By combining the above information with the cross-section calculation previously discussed, one can make a formal estimate of the rate of events per day, assuming that the crystal is precisely aligned with the incoming neutrino beam. For the ^{163}Ho case, being an unstable isotope, we can only assume a small quantity could effectively be used for a detector. Hence, we consider simply 1 mg of target material (equivalent to 240 μCi). Osmium is a better target due from these considerations in that it is stable (with an abundance of 1.56%). However, the reduced cross-section requires far more target mass than its holmium counterpart. Therefore, we consider a mass of 50 g for such a detector. Results on events/day are listed in Table IV. It is possible, in principle, to enhance the rate of each target by either tuning the crystal spacing to match the resonance exactly or by enhancing the target abundance. The enhanced rate due to these improvements is also listed in Table IV.

IV. EXPERIMENTAL CONSIDERATIONS

In order to realize an experiment capable of detecting solar anti-neutrinos in the scheme proposed in this article, a number of conditions must be simultaneously satisfied:

1. Sufficient quantities of the target material must be available.

2. The crystal must be able to serve not just as the target for the interaction, but also as the detector, since the energies of the electron are low enough that they would be almost immediately be absorbed.

3. The crystal must be orientable toward the source (i.e. track the sun's path across the sky).

4. It is desirable to calibrate the crystal orientation in situ.

We concentrate for the moment on the holmium target option. With regard to requirement #1, we benefit greatly from the fact that ^{163}Ho has been recently been the subject of study for the purpose of neutrino mass measurements. Production of the isotope usually stems from the irradiation of ^{nat}Dy from protons or alphas, or from the neutron bombardment of ^{162}Er. Quantities of the order of 10^{18} have been produced so far [?], an indicator that milligram quantities of the isotope are indeed feasible. Furthermore, such targets are used in conjunction with low energy bolometers with extremely high energy resolution. As such, such bolometric detectors simultaneously fulfill the requirements 1 and 2 within a single detector system. Such detector systems operate at milli-kelvin temperatures, which also contributes to the crystal uniformity.

Requirement #3 is far more challenging, particularly for cryogenic systems, as the crystal must be made to orient itself in the direction of the sun and track its position across the sky. Dilution refrigerators may be too cumbersome for such a task; however, adiabatic demagnetization refrigerators appear more suitable, given they are typically more compact and easily maneuverable. If properly mounted, the chassis of the detector system can be made to track the sun to better than a few arc seconds (assuming active feedback for position and orientation). The accuracy need not exceed this requirement, since the beam profile itself has an inherent smearing due to the fact that the neutrino source is distributed up to 0.1 solar radii from the center of the sun.

Another challenge is measuring the crystal orientation itself. Here, we can take advantage of x-ray diffraction crystallography to help calibrate and align the crystal properly. Consider, for example, the presence of a well-collimated x-ray source, with incoming (outgoing) momentum $\vec{k}_\gamma$ ($\vec{k}'_\gamma$), whose direction is known with respect to the neutrino (solar) beam (see Fig. 4). If both the photon energy and diffraction angle are then measured, the location of the Bragg peaks map directly to the neutrino energy where the crystal enhancement is expected to occur.

$$\vec{p}_\nu \underset{\vec{G}_{hkl}}{\equiv} \vec{k}_\gamma - \vec{k}'_\gamma \qquad (29)$$

Such a system would provide an in-situ calibration of both the crystal orientation and the neutrino energy. The calibration may require the target to rotate with respect to the x-ray source and secondary detector, complicating cryogenic operation. Given the crystal spacing may be subject to pressure and temperature variations, having an in-situ calibration of the crystal spacing is highly desirable.

Perhaps more difficult to realize would be the ability to slightly alter or *tune* the crystal spacing so as to match the crystal lattice to the desired energy resonance. Indeed, both osmium and holmium have been studied using diamond anvils and pressure-dependent curves for osmium have been measured. The complexity of using such high pressure delivery devices in combination with the detector readout have not been explored.

V. SUMMARY AND FORECAST

We have presented a possible scheme for detecting extremely low energy anti-neutrinos created in the core of the sun. If realized, such an experiment would be one of the smallest solar neutrino detectors ever constructed. We believe that the approach presented here opens the

TABLE III. Crystal orientations that most closely match the resonance neutrino capture energy of reaction 3. Only orientations with a non-zero structure factor are listed. The table also lists the reciprocal momentum, $\vec{G}_h kl$, the equivalent neutrino energy, E_ν, and the difference between the two resonances. The signature photon energy and electron binding shell is also listed.

	Orientation (hkl)	$|\vec{G}_{hkl}|$ (keV)	E_ν (keV)	Δ_E (eV)	E_γ (keV) (shell)
^{163}Ho	(1,0,2)	5.959	6.026	-66.7	8.581 (L2)
^{187}Os	(2,1,2)	14.996	14.996	-0.14	12.527 (L1)
	(1,0,0)	5.236	5.151	+84.7	2.682 (M2)
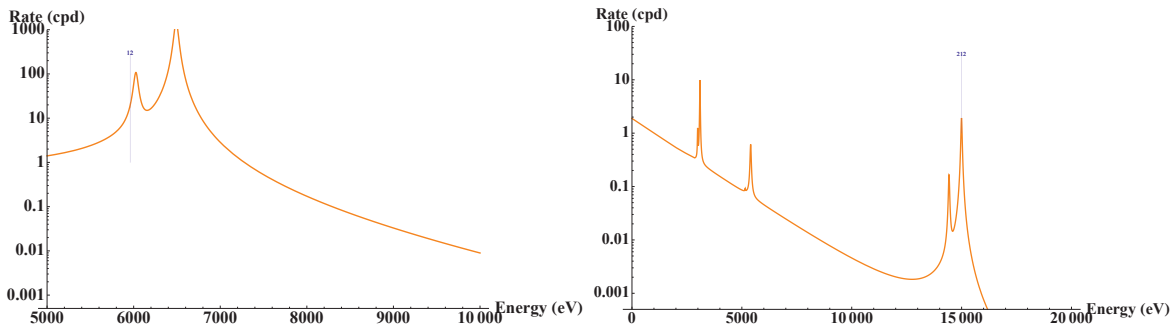
FIG. 3. The rate of resonance solar neutrino events per day for 1 mg of ^{163}Ho (left) and 50 g of ^{187}Os (right) assuming coherent scattering from a crystal. Blue line indicates location of closest crystal resonance.
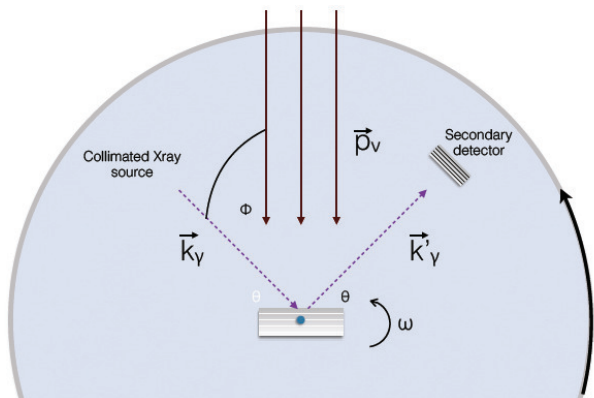
FIG. 4. A sketch of the proposed solar anti-neutrino detector, together with calibration scheme. Solar neutrinos enter with momentum $\vec{p}_\nu$, while x-rays from collimated source ($\vec{k}_\gamma$) arrive and Bragg scatter to a secondary detector with new direction $\vec{k}'_\gamma$. Both the Bragg scattering angle θ and the photon energy are measured to reconstruct the neutrino energy corresponding to the equivalent Bragg scatter (assuming the angle between the neutrino beam and x-ray source (Φ) is fixed and known. Both the source and the secondary detector are allowed to rotate about the central axis. The apparatus is assumed to be orientable along the solar axis plane.

door to a number of physics opportunities previously unexplored:

- If successful, the measurement would represent the first purely leptonic measurement of the temperature of the solar core. As such, the measurement would be nearly free of any uncertainties associated with nuclear cross-sections.

- The measurement would be a clean determination of the *vacuum* neutrino oscillation parameters in the solar sector, as the energies accessible to the measurement fall well below where MSW effects are present.

- It would represent the first demonstration of quantum collective behavior for neutrino-matter interactions.

Such a scheme wouldn't be feasible had not the source strength, lattice spacing, and nuclear details conspired in a favorable way. As such, the temptation of performing such a table-top neutrino physics may prove difficult to resist.

VI. ACKNOWLEDGEMENTS

TABLE IV. The calculated rate per day for 1 mg holmium or 50 g osmium detectors, assuming the incoming neutrino flux is aligned along the indicated crystal orientation. The enhanced rate due to tuning the crystal spacing and increasing the abundance to 100% (in the case of osmium) is also listed.

	Orientation (hkl)	Mass	Rate (d^{-1})	Enhanced rate (d^{-1})
^{163}Ho	(1,0,2)	1 mg (240 μCi)	13.8	101.5
^{187}Os	(2,1,2)	50 g	0.03	1.92
	(1,0,0)	–	8×10^{-7}	0.0026

Chapter 4

Multipurpose Beam Instrument for EIC

$$e \xrightarrow{B} \gamma e$$

Abstract

Parity violating electron scattering (PVES) is one the leading methods to probe physics beyond the Standard Model (SM). A large part of the physics program being envisioned for future facilities such as the EIC includes searching for physics beyond the SM. Here, we present a novel technique which uses the spacial asymmetry of SR produced by an electron beam passing through a wiggler magnet to trace the changes in beam polarization. Such a relative polarimeter could be vital if the goal of $< 0.5\%$ polarimetry is to be achieved at EIC. In this paper, we update the discussion on the development of this technique supported by a Geant4 simulation. The polarimeter apparatus along with the underlying basic ideas are briefly introduced. As a part of the simulation, the effects of electron beam current and beam energy were studied which were found to be manageable over a wide range of electron beam energies and beam currents. It was found that such a relative polarimeter works best in the $4 - 20$ GeV regime. When coupled with a CCD camera, the SR can be used to further monitor the beam profile as demonstrated at the Swiss Free Electron Laser (FEL). Furthermore, the SR can also be used to monitor the beam current and thus be effectively implemented as a beam current monitor. In the following chapter the extent of applicability of such a device is explored.

4.1 Introduction

This chapter is meant to bring forward developments since Ref. [55] was written, and in that spirit, only the most needed aspects are repeated here to keep the structure succinct. This work began as a project to develop a polarimeter but diversified to find

implementation in joint requirements of beam diagnostics, *viz.* beam profile monitor and beam current monitors.
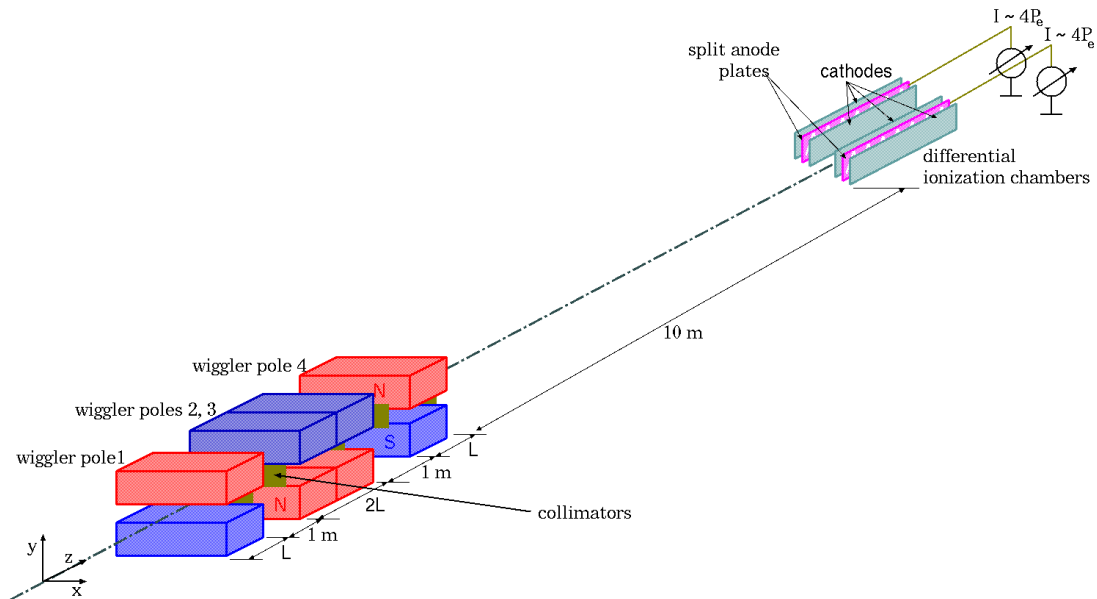
Figure 4-1: Schematic diagram of the SpinLight polarimeter apparatus.

PVES experiments of the future demand a high degree of precision in polarimetry which can only be achieved if more than one polarimeter is used. Therefore, new polarimetry techniques, besides the conventional Compton and Møller polarimeters, are required. Karabekov and Rosmanith had already come up with the idea of using SR to measure beam polarization [56]. Improving on the original proposal, the technique of the Spin-Light polarimeter here takes a step towards building a full fledged precision device. However, the power output of the wiggler magnets and resolution required to measure the spacial asymmetry of the SR produced by high energy beams constrains the electron beam energies at which such a polarimeter works best to below 20 GeV. A lower limit of 4 GeV on electron beam energies is imposed by the fact that at low energies, the spacial asymmetry of SR becomes SMall making it very difficult to measure the polarization.

4.2   Synchrotron Light

Sokolov et. al. [57] give the spin dependence of SR produced by an electron passing through a magnetic field in terms of convenient parameters including the SR photon's vertical opening angle - ψ (angle between the momentum component of the SR photon in the $y-z$ plane and the z axis) and its longitudinal polarization - ζ. One can obtain the power spectra (P_γ) by multiplying the number of SR photons (Eq (5.1)) with their corresponding energy. The difference of the integrated SR power spectra above (*i.e.* $0 \leq \psi \leq \pi/2$) and below (*i.e.* $-\pi/2 \leq \psi \leq 0$) the trajectory of the electrons turns out to be directly proportional to the longitudinal polarization of the electrons, with
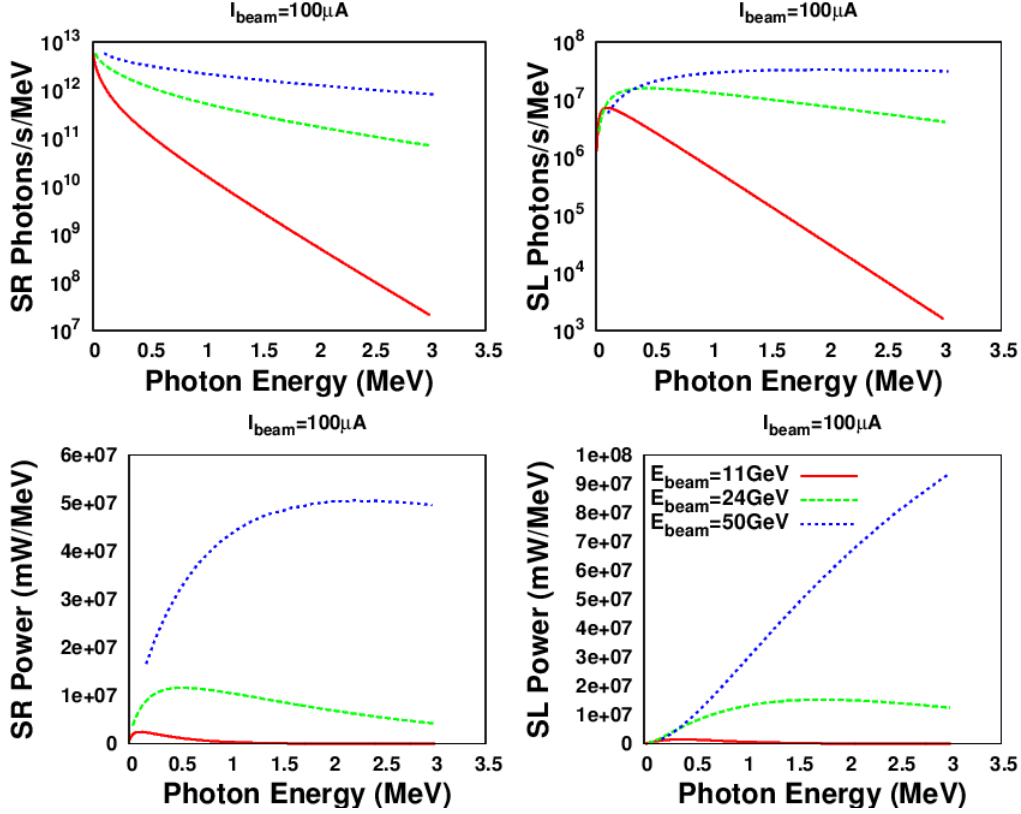
Figure 4-2: Figures showing SR & SL total number and total power spectra emitted by a wiggler magnet $B_{wig} = 4$ T carrying an electron beam current of 100 μA. Top: SR (Top-Left) and SL (Top-Right) photons per MeV as a function of electron beam energy.; Bottom: SR (Bottom-Left) and SL (Bottom-Right) power per MeV as a function of electron beam energy.

an offset term (P_{Unpol}) arising due to non-zero, but spin-independent, integrated (over all energies) power for a spin-averaged electron passing through a magnetic field. In this paper, the quantity in Eq. (5.1) is referred to as *spin-light* (SL) [61].

$$
N_\gamma = \frac{9n_e}{16\pi^3} \frac{e^2}{cm_e R^2} \gamma^4 \int_0^\infty dy \frac{y^2}{(1+\xi y)^4} \oint d\Omega (1+\alpha^2)^2 \times
$$
$$
\left[K_{2/3}^2(z) + \frac{\alpha^2}{1+\alpha^2} K_{1/3}^2(z) + \zeta\xi y \frac{\alpha}{\sqrt{1+\alpha^2}} K_{1/3}(z)K_{2/3}(z) \right] \qquad (4.1)
$$

$$
\Delta P_\gamma = P_{Pol} - P_{Unpol} = -\zeta\xi P_{Clas} \int_0^\infty dy \frac{9\sqrt{3}}{8\pi} y^2 K_{1/3}(y) \qquad (4.2)
$$

where $\xi = 3B_{wig}/(2B_c)$, B_c being the magnetic field under the influence of which the entire kinetic energy of the electron is expelled as one SR photon, $y = \omega/\omega_c$, $K_n(x)$ are modified Bessel functions, n_e is the number of electrons and, $z = \omega(1+\alpha^2)^{3/2}/(2\omega_C)$,
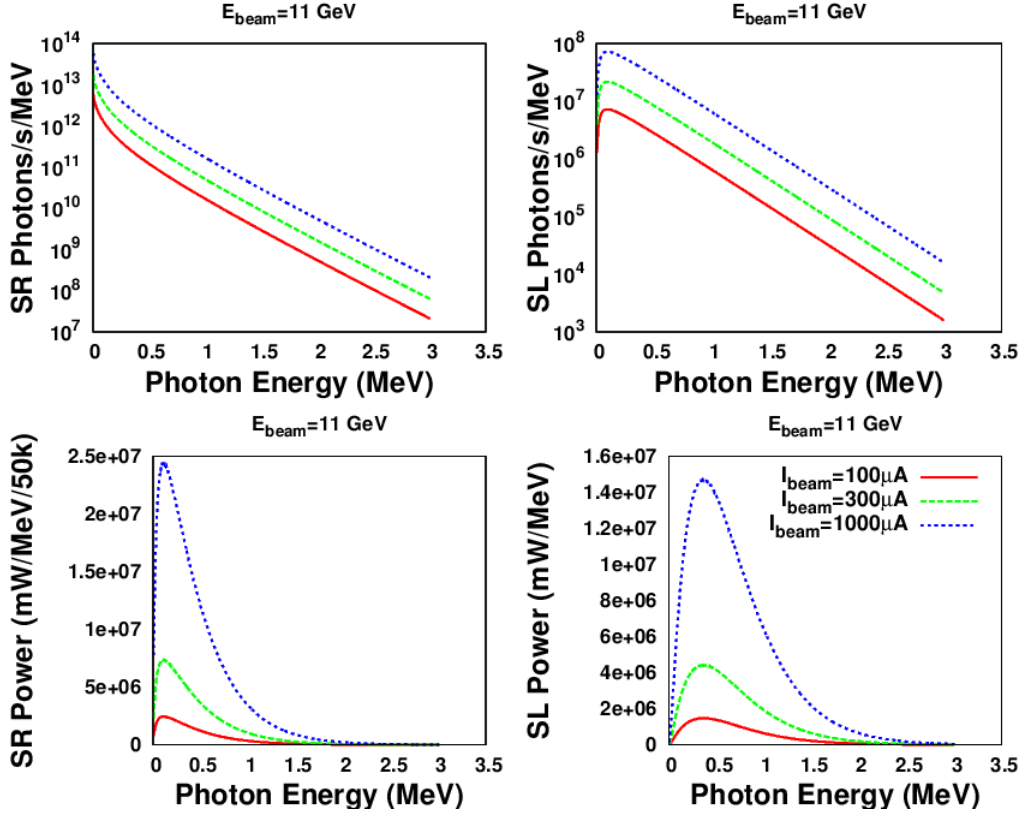
Figure 4-3: Figures showing SR & SL total number and total power spectra emitted by a wiggler magnet $B_{wig} = 4$ T carrying an electron beam with an energy of 11 GeV. Top: SR (Top-Left) and SL (Top-Right) photons per MeV as a function of electron beam current.; Bottom: SR (Bottom-Left) and SL (Bottom-Right) power per MeV as a function of electron beam current.

and $\alpha = \gamma\psi$. An asymmetry term, $A = \Delta N_\gamma / N_\gamma$ can then be defined from the above two equations, where ΔN_γ corresponds to ΔP_γ.

4.3 Spin-Light Polarimeter

A most basic layout of the spin-light polarimeter would include a 3-pole wiggler magnet, collimators and a split plane IC as illustrated in Figure 4-1[58].

4.3.1 Wiggler Magnets and Collimators

When an electron beam passes through a set of three wiggler (chicane like) magnets, where the central pole is twice as long as the poles on the extremes, the electron beam produces SR photons which contains the beam polarization information. All the individual magnetic poles would have equal field strength but the direction of the field of the central pole would be opposite to that of the poles on the extremes so that the electron beam direction ultimately remains unchanged. The magnetic field

strength of 4 T corresponding to a pole length of about 10 cm, which gives a SR fan spread of about 1 mrad in ψ (vertical angle), was chosen owing to the availability of magnets with similar field strength. The effects of such wiggler magnets on the quality of the electron beam was studied in Ref. [58] and was reported to be negligible. Collimator slits in front of both the faces (faces through which the beam enters and exits the wiggler poles) of each wiggler magnet pole allows collimation of the SR beams, as illustrated in Figure 4-4, and directs them to two identical split-plane ICs, one each on beam right and beam left positions down the beam-line from the wiggler magnets. With the help of collimators (yellow strips in Figure 4-4), one narrow beam of SR photons can be extracted from each wiggler pole, numbered 1 through 4. Of the four narrow beams extracted with the help of collimators, two of the narrow beams are directed to one IC while the other two narrow beams are directed to the other ICs.
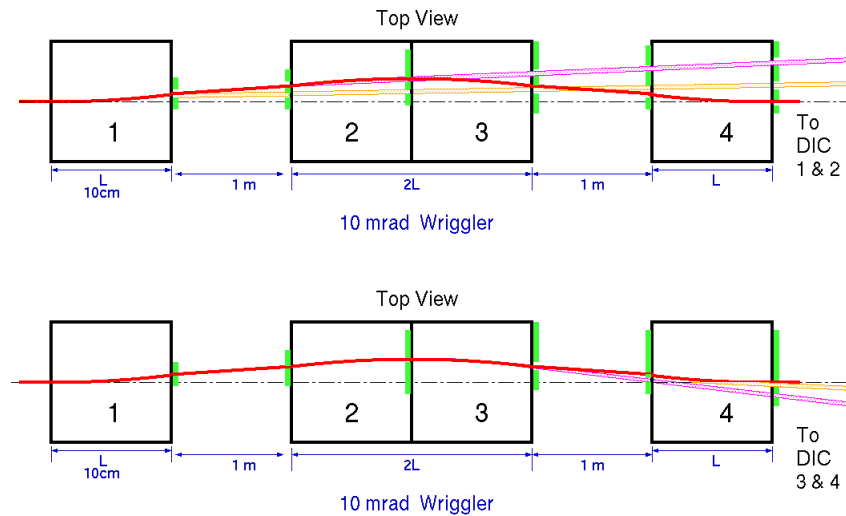
Figure 4-4: Top: Schematic diagram showing the location of collimators (yellow strips) on the wiggler pole faces which guide the SR photons produced at the wiggler magnet to the beam left IC.; Bottom: Schematic diagram showing the location of collimators on the wiggler pole faces which guide the SR photons produced at the wiggler magnet to the beam right IC.

Notice that the collimators truncate the SR fan produced at the wigglers in an angle-ϕ (angle between the momentum component of the SR photon in the $x-z$ plane and the z axis), which is orthogonal to the angle-ψ, where SR photon distribution in ψ contains the electron beam polarization information. Another important design consideration is the amount of time required to achieve statistically sufficient data which is inversely proportional to the product of asymmetry and the SR flux reaching the IC after collimation. In Figure 1-5Right, a plot of the amount of time required to obtain 1% uncertainty in polarization measured as a function of magnetic field indicated that only about 10 minutes are required if the wigglers were operated at a field strength of 4 T, a fairly plausible time scale for each measurement.

4.3.2   Spin-Light Characteristics
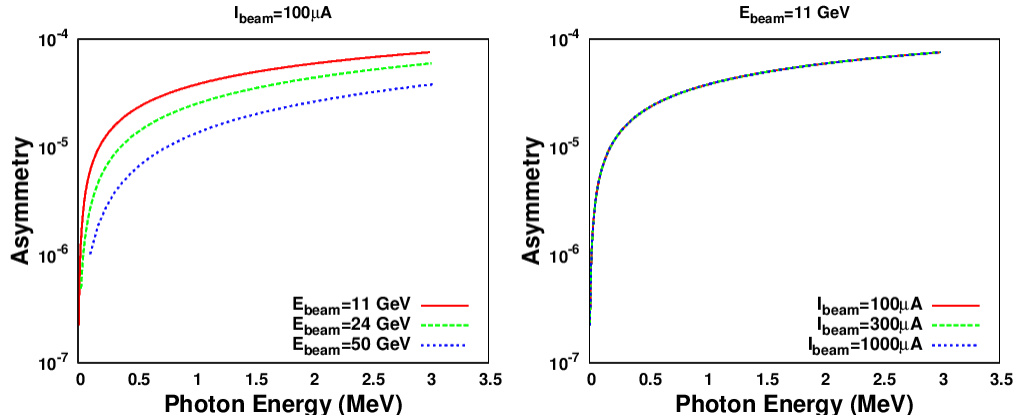
Figure 4-5: Left: A plot of asymmetry in the SR light fan as a function of the SR photon energy for various electron beam energies and a fixed electron beam current of 100 μA.; Right: A plot of asymmetry in the SR light fan as a function of the SR photon energy for various electron beam currents and a fixed electron beam energy of 11 GeV.

Now that the parameters of the apparatus that generates SR photons are fixed, we can look at the charecteristics of SL photons in contrast to that of SR photons. Eq. (5.1) can be numerically integrated to plot the SR & SL number spectra as a function of photon energy, while the SR & SL power spectra could then be obtained from the corresponding number spectra as illustrated in Figures 4-2 & 4-3. In Figures 4-2 & 4-3, the plots have been made for various electron beam energies holding the electron beam current constant at 100 μA and for various electron beam currents holding the electron beam energy constant at 11 GeV respectively. Similarly, by numerically integrating Eq. (5.2), one could plot the asymmetry in the SR fan as illustrated in Figure 4-5. An observation of interest here would be that while there is a slight drop in overall asymmetry with increase in electron beam energy, the asymmetry distribution effectively remains unchanged over a wide range of electron beam currents.
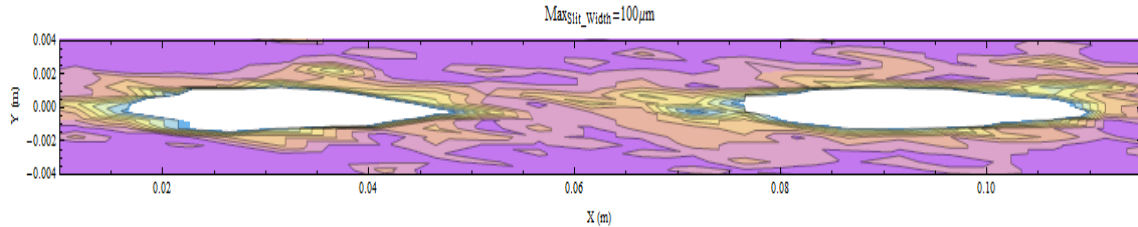
Figure 4-6: 2D projection of the collimated SR distribution in the ionization chamber as generated by the Geant4 simulation, the lighter areas have higher flux.
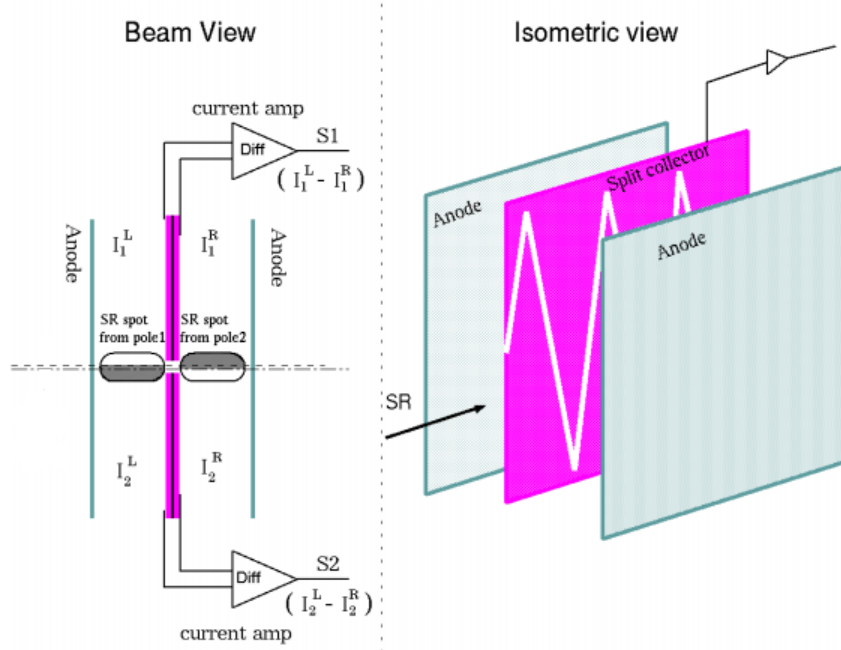
Figure 4-7: Left: A schematic diagram of the two collimated narrow SR beams (ovals) incident on beam left split plane ICs.; Right: An isometric view of the split plane IC showing the back-gammon like central cathode sandwiched between two anodes.

4.3.3   IC

The IC required for a spin-light polarimeter need to be sensitive to the fine spacial asymmetry of the collimated SR beam reaching the IC, *i.e.*, the IC must be able to count the SR photons along with position information. According to Eq. (5.1), only the difference between the total flux of SR photons, within the collimated SR beam ovals, above and below the plane of motion of electrons is of interest. Figure 4-7Left illustrates this fact by shading a portion of each SR beam oval indicating a lower flux of SR photons in that region compared to the unshaded region of the oval. With the help of an IC using central split-plane cathode, as illustrated in Figure 4-7, can pick out such up-down asymmetry and the signal $I_1^{L,R} - I_2^{L,R}$ will then be directly proportional to electron beam polarization. But by using the signal $S1 - S2$, also directly proportional to the electron beam polarization, one could eliminate issues introduced by vertical electron beam motion [58]. The fact that the signal $S1 - S2$ is only directly proportional to the electron beam polarization makes this setup, at best, a good differential polarimeter.

To study the IC response and behavior, a full fledged Geant4 [60] simulation of the entire spin-light apparatus was built and its validation is presented in Ref. [59]. The SR beam ovals indicated in Figure 4-7Left was regenerated in Geant4 using collimator slit width of 100 μm and is presented in Figure 4-6. Given that the SR cone has a 1 mrad angular spread, the ovals in Figure 4-6 has a rough semi-major axis of 1 cm with the distance between the wiggler magnets and the IC being about 10 m. IC characteristic response time could be defined as time required to reach $1/e$ of the
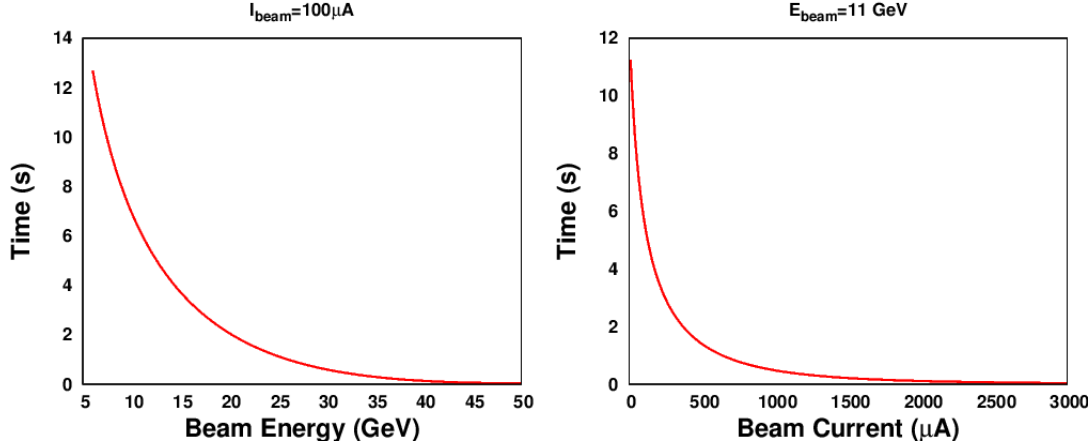
Figure 4-8: Left: A plot of response time of the IC as a function of electron beam energy held at a fixed electron beam current of 100 μA.; Right: A plot of response time of the IC as a function of electron beam current held at a fixed electron beam energy of 11 GeV.

maximum current $(I_{1,2}^{L,R})$ that the IC can provide before the IC saturates, when a collimated SR beam, produced by well defined electron beam, is incident on the IC. Figure 4-8 plots this response time for a ICs with dimensions 1 m $z-axis \times$ 10 cm $\times$ 10 cm filled with Xenon gas at 1 ATM pressure. While it is usual to observe a quick drop in response time of IC as electron beam energy increases, it is important to note that the response time falls quickly even as electron beam current increases. Even though one would naively expect a linear decay in response time with increase in electron beam current, one must note that that SR beam power spectra changes significantly with change in electron beam current (as illustrated in Figure 4-3Left & Right leading to quick decay in response time with increasing electron beam current. Finally, with the help of Geant4, the effect of addition of a realistic beam halo, with a one - thousandth peak amplitude as compares to the peak amplitude of the cylindrical Gaussian beam, can be studied. In Figure 4-9, the difference in asymmetry with and without the above mentioned halo is presented.

4.4   SR Transverse BPM

Given that SR photons have a fixed angular distribution given in Eq. (5.1), it could also be used to measure the beam sizes in a transverse plane. The angular spread of an SR cone is easy to calculate given the magnetic field of the bending magnets (where the SR light was produced) and the path length of the beam in the magnetic field [55]. Physical distribution of SR photons directly corresponds to the transverse size of the beam. If the angular spread of the SR cone is δ rad, and the screen is very close (a distance d) to the SR light source such that δd is much less than the transverse beam size, the size of SR beam spot is directly proportional to the transverse beam size. In case δd is not negligible compared to the transverse beam size, then the
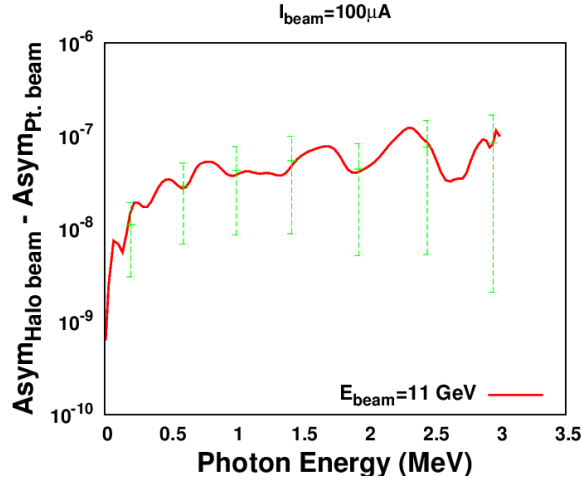
Figure 4-9: A plot showing the difference in asymmetry introduced by the addition of a beam halo generated using the Geant4 simulation.

proportionality would still hold between transverse beam size and the bunch SR beam spot from which the single electron fringe SR contribution is subtracted. This direct proportionality allows for measurement of the transverse beam profile without counting a large number of SR photons. Naively, just one SR photon per electron in the bunch is required to map out the beam.

4.4.1 CCD as Photon Imaging Device

CCD could be used to image the SR cone of the light current is within tolerances of the CCD. This was not possible for the previous case study involving the relative Spin-Light polarimeter since the test flux of SR photons was very high. Usually in case of beam profile monitors where statistics is not a concern the current of SR light can be dampened so as to be within the tolerance of the CCD camera. Dampening SR beam was not an option in the case of a relative polarimeter where a large number of photons had to be counted in order to achieve high precision polarimetry. In case of Figure 4-10, the beam size is near about perfectly the same size as the imaged SR beam spot, since the CCD is very close to the SR source.

Since asymmetry gives a rough measure of how well an imaging device could resolve the spatial distribution, it is important to study the dependence of asymmetry w.r.t. to the size of CCD pixels. For this purpose, the Geant4 was modified to include a CCD camera in the place of an IC and each pixel was digitized in the simulation, keeping simulation numerical resolution in mind to be always far superior to the pixel sizes used for the study. One would expect that if the entire CCD camera were made of just one pixel, the asymmetry that such a CCD camera could measure would always be 0 and in the limit of pixel size tending to infinitesimally SMall, the asymmetry would approach 1 exponentially. In the limit of pixel size tending to infinitesimally SMall, each photon impinging on the CCD camera is registered by a single pixel, therefore giving perfect position resolution. In case of an extended pixel size, the

49
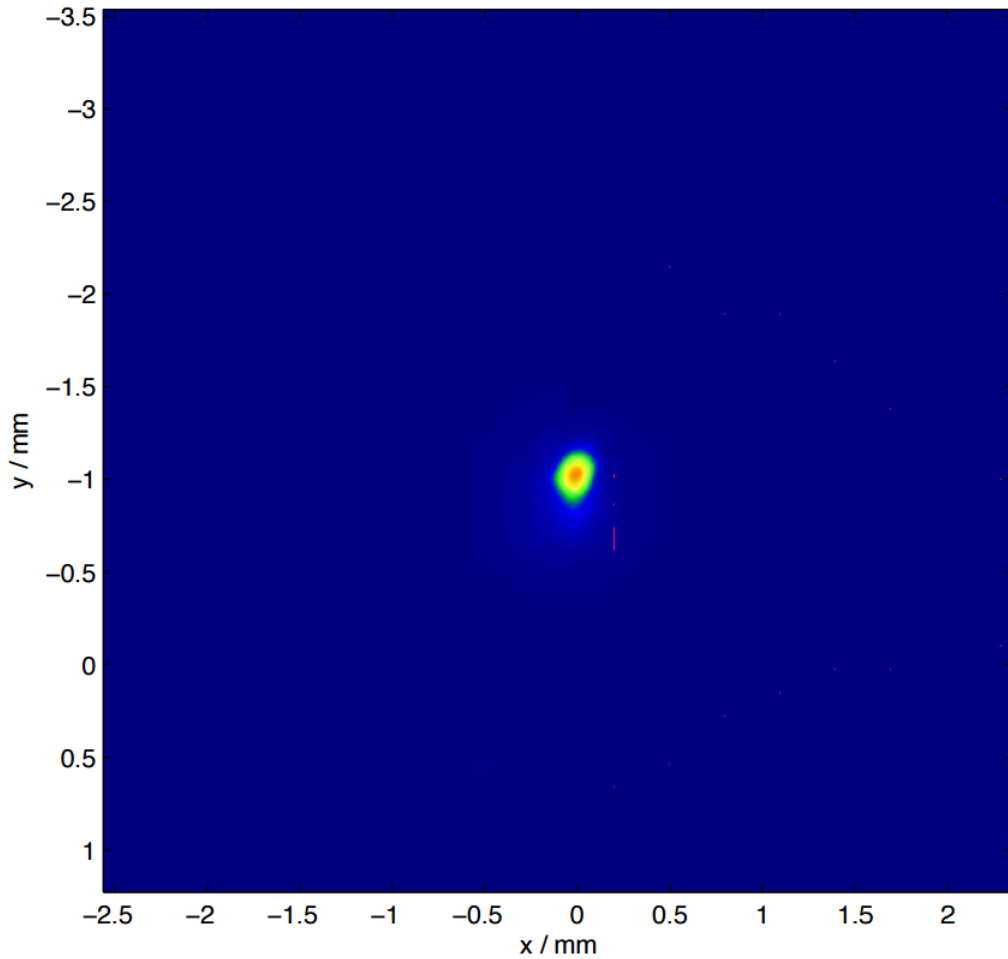
Figure 4-10: Sample SR Beam Spot produced by the Swiss Free Electron Injector beam with $E_{beam} = 250\text{MeV}$ & $B_{wig} = 0.4\text{T}$ with a CCD screen located 10cm from the SR source.
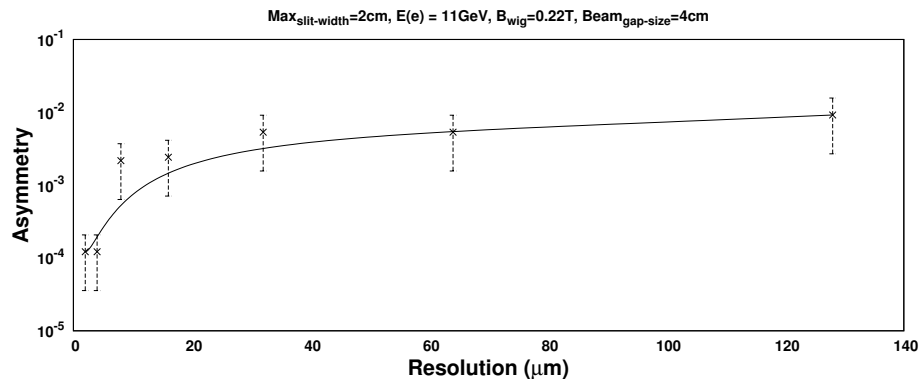
Figure 4-11: Plot showing best asymmetry measurable as a function of pixel size using an electro beam $E_{beam} = 11$ GeV & $B_{wiggler} = 0.22$ T.

number of photons recorded is a integral of Eq. (2.1) over some SMall solid angle. The asymmetry is then measured as an averaging of a sum total of the readings from each pixel which introduces greater errors. The zero line is set ($\psi = 0$) with a precision of one pixel size. Since most SR photons are close to the zero vertical angle, best possible measurement of asymmetry is constrained by the error in counting photons that belong to $-\pi/2 < \psi < 0$ and $0 < \psi < \pi/2$. This effect was studied discretely using an 11 GeV electron beam producing SR photons at a magnet with 0.22 T field and where the CCDs located at a distance of 10 m from the SR source. Figure 4-11 demonstrates the dependence of the best measurable asymmetry with the size of pixels in the CCD.

4.4.2 Proof of concept BPM at SITF
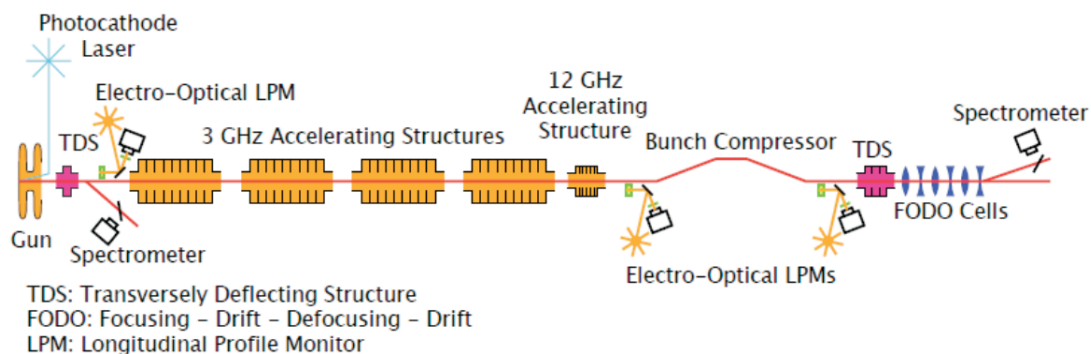
Figure 4-12: Schematic diagram of the SITF.

Swiss FEL Injector Test Facility, is a 250 MeV electron beam test bed for testing and gaining experience with new beam diagnostics being developed for the main Swiss FEL project which aims towards the construction of a 5.8 GeV electron linac driven coherent FEL light source of wavelength in the ranges of $0.1 - 0.7$ nm and $0.7 - 7$ nm. The SITF currently operates with $10 - 200$ pC, up to 250 MeV electron bunches which are about 0.36 ps in length and at a repetition rate of about 10 Hz [64]. As illustrated in Figure 4-12, the compact SITF beam line consists of tunable ultra violet laser operated photoelectric electron gun. The laser is pulsed in order to achieve the design longitudinal size of electron bunches. Within the electron gun, the electrons achieve an energy of about 7.1 MeV. These electrons are then accelerated by 4 S-Band, 3 GHz traveling wave RF cavities to operational maximum of 250 MeV. The X-Band, 12 GHz cavity was not used in these tests. Following the accelerating cavities is a 4-dipole chicane which are each capable of 0.4 T field and are of 25 cm pole length [68]. A couple of well placed Transverse Deflecting Cavities and a series of Focusing - Drift - Defocusing - Drift system consisting of a series of solenoids and SMall dipoles corrected with quadrupoles are used to control beam optics and measure longitudinal bunch length using streaked cameras to compare against the pulse rate of the electron gun laser. Finally the beam line consists of a spectrometer capable of resolving energy

to 1%. Repeated studies have shown that a high quality of beam, with emittance of about 0.65/0.25 mm.mrad, can be produced and maintained through the accelerating cavities and beam optics [65] [66].
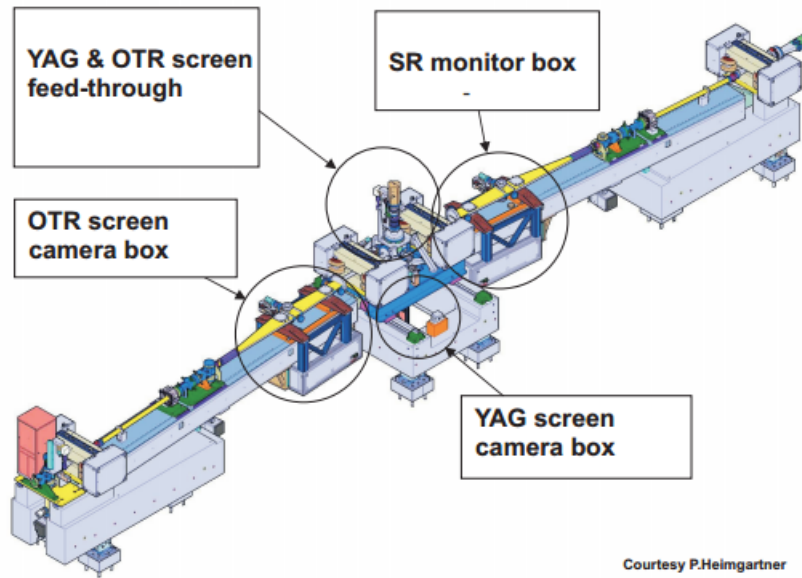
Figure 4-13: Schematic of the Bunch Compressor Assembly at the SITF showing the three different beam profile monitors, *viz.* OTR Screen, YAG Screen and SR Profile Monitor.

One region in the accelerator of great interest to this study is the bunch compressor chicane capable of producing synchrotron light. Figure 4-13 shows this region in great detail along with other diagnostics installed within, all geared towards profiling the beam in the transverse plane. The position of the beam in the chicane is located by resonant strip line Beam Position Monitor (BPoM) with an accuracy of 7μm and the time sensitive instrument in the chicane are triggered by a Beam Arrival Monitor (BAM) which is accurate up to 5 ps [67]. There are two obstructive means of measuring the transverse beam profile on the chicane. One being the YAG scintillator screen and the other being the OTR screen. Cerium doped YAG screen scintillates with a 530nm light when an appropriate energy electron strikes it, where as the light from the ultra thin foil of tin used as an OTR screen originates from charged particles (electrons) transiting between media (vacuum and tin) with different dielectric constants. Both of these screens are simply inserted into the beam and the light coming from these screens is imaged using a very high speed PCO ™ Edge [62] CCD camera. Both YAG and OTR screens therefore tend to be invasive and interfere with beam optics detectable down the beam line. Thus they are only inserted into the beam for a quick invasive measurement. The synchrotron light from the third dipole is also imaged using a camera. The synchrotron light method of measuring the transverse profile is however a non invasive means. The SR monitor therefore can be used continuously

and is only limited by the resolution and speed of the camera used.
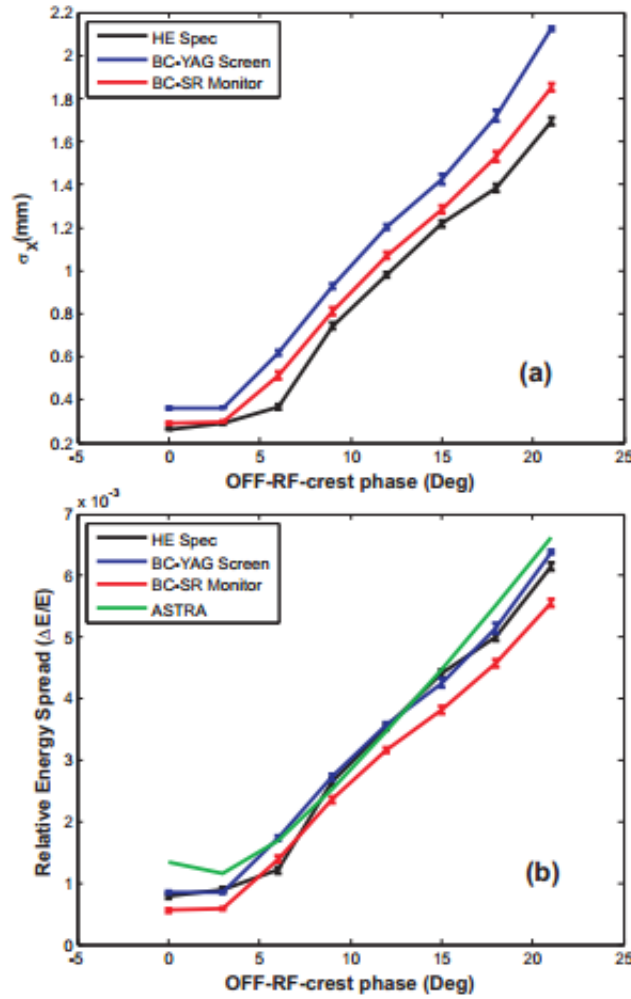
Figure 4-14: Top: Plot showing comparison of transverse bunch size as a function of location of the beam, w.r.t. to the RF accelerating pulse, obtained by the three different beam profile monitors. Bottom: Plot showing a comparison of energy spread of the bunch as a function of location of the beam, w.r.t. to the RF accelerating pulse, obtained by the three different beam profile monitors [63].

The profile of light imaged by the YAG and OTR screens is literally a time slice of the transverse beam profile. Since the SR monitor camera is located very close to the SR source, beam divergence is negligible compared to the size of the beam itself and so the profile of light imaged by the SR monitor camera is also literally a time slice of the transverse beam profile. One would think the profile measured by these means should align together. The image obtained from the SR monitor camera is fit to a 2D Gaussian curve and the mean diameter of the distribution is reported as beam size σ_x. Relative energy spread (ΔE) can also be calculated easily using the mean beam size [63];

$$\sigma_x = \sqrt{\sigma_{x,0}^2 + \left(\eta_x \frac{\Delta E}{E}\right)^2} \qquad (4.3)$$

where $\sigma_{x,0}$ is the natural betatron size of the electron beam and η_x is the horizontal dispersion of the chicane.

Each bunch sits nominally off crest to ride the RF pulse in the accelerator and therefore the Figure 4-14 shows transverse beam sizes obtained from each of the three beam profile monitors as a function of off-RF crest phase. Values of transverse beam size were calculated from images captured at a time interval ($\sim$ 1 ps) equal to a very SMall fraction of the S-Band cavity accelerator frequency (3 GHz). It is interesting to note that each of them measures similar transverse beam sizes. SMall differences arise due the the fact that the SR monitor was not aligned and the SR cone dispersion was not included in calculation of error bars. Also the readings obtained come from different locations on the SITF. Even though previous studies have shown the system conserves beam quality, the margin of acceptance of beam quality was not included in the calculation of the error bars presented in Figure 4-14.

4.4.3 BPM at EIC
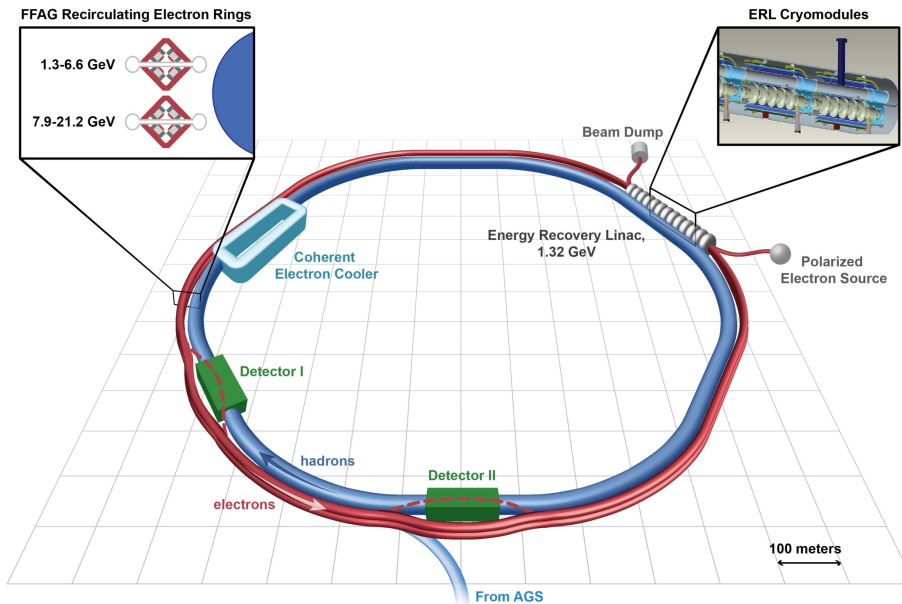
Figure 4-15: Schematic diagram of the Electron Relativistic Heavy Ion Collider (eRHIC), and EIC proposal.

At eRHIC, the electron recirculating ring is filled with an electron beam with much different characteristics than in the Linac at SITF. At eRHIC, a the recirculating rings

hold circulating electron beams of different energies in the same beam pipe. However, the bunches of different energies are spatially separated owing to electrons of different energies having different orbits. Ideally, at eRHIC, the recirculating ring is filled with bunch-trains of 110ns long with 42 bunches, each bunch with about 5.3nC of bunch charge. This translates to about $222\mu C$ in bunch-train charge. Also the electron bunch-trains have a repetition rate of 9.38 MHz which means that there is a gap of about 110 ns between two 110 ns long bunches (head to toe) [69].
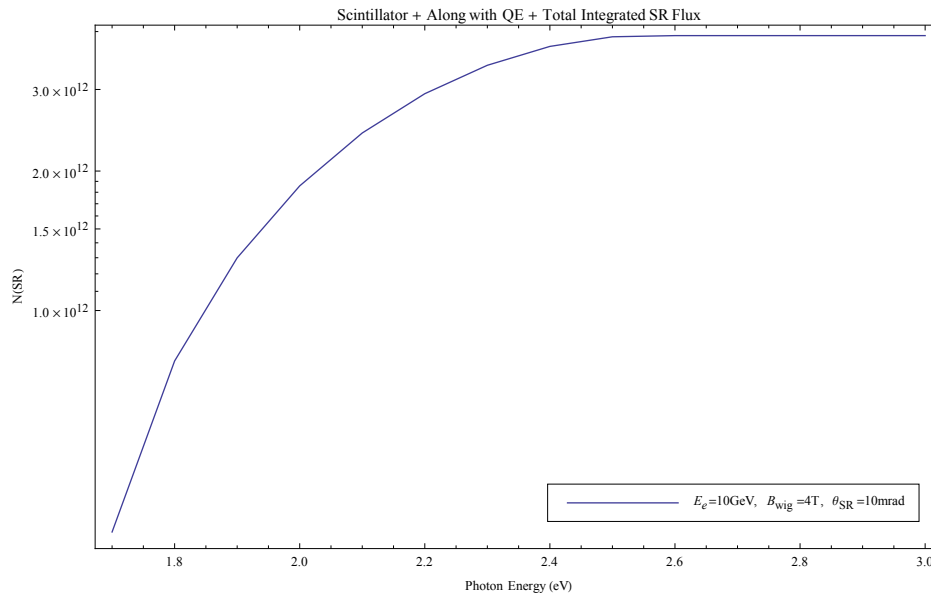
Figure 4-16: Plot showing total effective number of photons available as a convolution of the quantum efficiency of the PCO ™ Edge [62] CCD camera and scintillation photons generated by a scintillator upon which SR photons generated at the 4 T wiggler magnet by a 10 GeV electron beam are incident.

We can implement a SR Transverse BPM here borrowing on the lessons learnt at the SITF. The eRHIC SR beam profile monitor would look similar to the one depicted in Figure 4-13, but would involve a 4 T dipole - chicane instead. The SR light output could be wavelength shifted from original X-Ray to visible spectra using a scintillator such as the one mentioned in Ref. [70]. Coupled with a camera with about 10^4 pixels and taking into account the camera's quantum efficiency, one could arrive at an effective SR - Scintillator photon spectra available for measurement. Notice that Figure 4-16 samples 1s in time and provides SR-Scintillator flux per pixel of camera, which means each bunch-train which have a length of about 110 ns has roughly in excess of 10^5 photons at all available spectral energies. This opens up the possibility for measuring the beam profile of each bunch which reduces the available photon flux roughly around 2500 photons/pixel/bunch.

4.5   SR Beam Current Monitor

The rate change of the total integrated intensity of transverse beam profile gives a measure of beam current. This invariably requires very high precision BAM in order to trigger the beam profile monitors. The two separate entities required to make this work would be the high resolution SR imaging and high prevision timing. High resolution SR imaging has been shown to be reliable means of measuring transverse beam profile in *Section 5.4.2*. Reliability of BAM has been known to be better than 5 ps as well. Given that each bunch stretches for about 2.5 ns, it would be feasible to implement a triggered system in order to obtain a bunch by bunch beam current measurement accurately. An averaging beam current monitor could naturally evolve out of a bunch by bunch monitor to measure bunch-train currents and many bunch-trains' averages.

4.6   Conclusion

The spin-light polarimetry technique presents a novel method which is not just capable of achieving a high degree of precision, but is also a non - invasive and continuous technique. Such a polarimeter could ideally be implemented as a differential polarimeter which could easily be operated in series with Compton or Møller polarimeters. The SMall response time of the IC indicates that it will have to be operated with a duty cycle of less than 100% in order to allow it to recover from saturation. This adds overages to the time required to obtain 1% statistics but owing to SMall recovery times (similar to response time) and SMall statistical run time requirement, this is not debilitating. Ref.[58], tabulates a number of systematic uncertainty sources. To that list, one might add a maximum halo contribution of about 0.1% owing to a residual asymmetry of about 10^{-7} compared to the halo less asymmetry of 10^{-4}. Table 4.1 lists possible contributions to sources of error in a SR based beam diagnostic but to precisely list all the sources of errors is nevertheless a challenge.

Table 4.1: Systematic uncertainties in a SR based beam diagnostic

Source	uncertainty	$\delta A/A$ (%)
Dark current	$\sim$ pA	< 0.01
Intensity fluctuations	$\Delta N \times 10^{-3}$	< 0.1
Beam energy	1.0×10^{-3}	< 0.05
Density of chamber gas,	relative difference	< 0.01
slit width	100 μm	< 0.2
Background related	known to $\sim 0.5\%$	~ 0.5
Dilutions	with B/S $\sim 0.5\%$	~ 0.5
other dilutions	cancel to first order	< 0.1

It has been established that SR beam profile monitors could give an accurate way

to characterize beam profile in 3D at the SITF. However to adapt the technology to the demands of the eRHIC EIC plan remains an active R & D project in progress. More over such a non invasive device with its numerous applicability could add to the other beam diagnostics to produce a means to measure the beam parameters redundantly, a prerequisite of all modern accelerator systems.

Appendix A

Addendum to Section 1.3

Scaling the invariant cross section for Compton scattering, as mentioned in Ref. [12], with $\eta(\omega)^{-1}$ introduces refractive index into the cross section expression as;

$$\frac{d\sigma_c}{dy} = \frac{\pi r_e^2}{x\eta(\omega)}\left(\frac{1}{1-y} + (1-y) - 4r(1-r)\right) \tag{A.1}$$

$$\frac{d\sigma_\lambda}{dy} = \frac{\pi r_e^2}{x\eta(\omega)}u \tag{A.2}$$

where, r_e is the classical electron radius, λ is the product of electron and photon beam polarizations, $r = y/(x - xy)$, $u = rx(1-2r)(2-y)$, $y = 1 - (p_0k/p_0k_0)$, and $\eta(\omega) = (n^2 + n\omega(dn/d\omega))$. Here p_0 refers to the 4-momentum of the initial electron and $k_0(k)$ refers to the 4-momentum of the initial(final) photons. Finally, $x = 2p_0k_0/m_e^2$, and $p_0k \approx (\epsilon_0\omega/2)((1/\gamma_0^2) + \theta^2 + 2(1-n))$. The sub-0 terms belong to the initial state electron or photon and the terms without sub-0 refer to the final state electron or photon. The θ terms could then be eliminated by using the following relations along with conservation of energy in Compton scattering [7].

$$n - 1 = \frac{1}{2\gamma_0^2}\left(1 + \theta^2\gamma_0^2 - x\left(\frac{\epsilon_0}{\omega} - 1\right)\right) \tag{A.3}$$

$$x = \frac{4\gamma_0\omega_0 sin^2(\theta_0^2/2)}{m_e} \tag{A.4}$$

The asymmetry (A) as mentioned in Eq. (3) can also be expressed as a product of λ and an analyzing power (I_λ/I_c) as follows:

$$A = \lambda\frac{I_\lambda}{I_c} \tag{A.5}$$

where, $I_{\lambda(c)} = \int_{\epsilon_{min}}^{\epsilon_{max}} \epsilon(d\sigma_{\lambda(c)}/d\epsilon)d\epsilon$ and $\epsilon_{min(max)} = c_0(S_N + (-)D/2 + S - S_c)^{-1}$. Here $c_0 = 296.45$ GeV cm and for JLab Compton polarimeter, base distance offset of the first channel (strip) on the electron detector from the beam line, $S = ?$, channel size $D = ?$, the distance offset of the Nth channel from the first strip $S_N = DN$cm and S_c is the Compton kinematic endpoint. Putting it all together an expression for

59

asymmetry (A) w.r.t to the photon energy (ω_0) leaves us with 3 free parameters, viz. S_c, n and λ.

Appendix B

Bibliography

[1] C. S. Wu et. al., Physical Review **105** 4: 1413âĂŞ1415 (1957).

[2] J. H. Christenson, J. W. Cronin, V. L. Fitch, and R. Turlay, Phys. Rev. Lett. 13, 138

[3] O. W. Greenberg, Phys. Rev. Lett. **89**: 231602 (2002).

[4] S. Liberati, Class. Quantum Grav. **30**: 133001 (2013).

[5] V. A. KosteleckÃ¡ and N. Russell, Rev. Mod. Phys. **83** 11 (2011).

[6] W. Deconinck, Hyperfine Interactions **200** 1-3 (2011): 31-34.

[7] V. Gharibyan, Phys. Lett. B **611**, 231 (2011).

[8] F. W. Lipps and H. A. Tolhoek, Physica **20** 85: 385 (1954).

[9] V. Gharibyan, Phys. Rev. Lett. **109**: 141103 (2012).

[10] V. Gharibyan, arXiv:1401.3720

[11] S. C. Miller and R. M. Wilcox, Phys. Rev. Lett **124**, 3 (1961).

[12] I. F. Ginzburgm, et. al. , Nucl. Instrum. Methods A **219**, 5 (1984).

[13] R. C. King, SLAC Technical Report **0452**.

[14] V. A. Kostelecky and M. Mewes, Phys. Rev. D **66**, 056005 (2002).

[15] S. Coleman and S. L. Glashow, Phys. Lett. B **405**, (1997): 249.

[16] J. Wdowczyk and A. W. Wolfendale, Ann. Rev. Nucl. Part. Sci. **39**, (1989): 43.

[17] HEGRA Collaboration: A. Konopelko et al., Astropart. Phys. **4**, (1996): 199.

[18] Aharonian et al. (HESS Collaboration), Astron.Astrophys. **448** L 43-47 (2006).

[19] C. Akerlof et al., Nature **398**, (1999): 400.

[20] R. Salvaterra et al., Nature **461** , 1258-1260 (2009).

[21] D. Androic et al., Phys. Rev. Lett. 111, 141803 (2013).

[22] T. Allison et al., Nucl. Instr. Meth. A781,105 (2015).

[23] D. Gustavson et al., Nucl. Instr. Meth. **A165**, 177 (1979)

[24] L. Knudsen et al., Phys. Lett. **B270**, 97 (1991).

[25] D. P. Barber et al., Nucl. Instr. Meth. **A329**, 79 (1993).

[26] I. Passchier et al., Nucl. Instr. Meth. **A414**, 446 (1998).

[27] W. Franklin et al., AIP Conf.Proc. **675**, 1058 (2003).

[28] M. Baylac et al., Phys. Lett. **B539**, 8 (2002); N. Felletto et al., Nucl. Instr. Meth. **A459**, 412 (2001).

[29] M. Friend et al., Nucl. Instr. Meth. **A676**, 96 (2012).

[30] K. Abe et al., Phys. Rev. Lett. **84**, 5945 (2000); M. Woods, hep-ex/9611005 (1996).

[31] A. Acha et al. [HAPPEX Collab.], Phys. Rev. Lett. **98**, 032301 (2007).

[32] C. Bauer et al., Nucl. Instrum. Methods **367**, 207 (1995).

[33] M. M. Zoeller et al., IEEE Trans. Nucl. Sci. **44**, 815 (1997).

[34] A. Denner and S. Dittmaier, Nucl. Phys. **B540**, 58 (1999).

[35] M. A. Hohensee et al., Phys. Rev. Lett. **102**, 170402 (2009); Phys. Rev. **D 80**, 036010 (2009); B. D. Altschul, Phys. Rev. **D 80**, 091901(R) (2009).

[36] V. A. KoseleckyÂť and M. Mewes, Phys. Rev. Lett. **87**, 251304 (2001); Phys. Rev. **D 66**, 056005 (2002).

[37] R. D. Peccei and H. R. Quinn, Phys. Rev. Lett. **38**, 1440 (1977).

[38] J. Preskill, M. Wise, and F. Wilczek, Phys. Rev. Lett. **120B**, 127 (1983).

[39] H. Baer, Particle Physics and Cosmology Meeting (PPC2013), (2013): arXiv.org: 1310.1859 .

[40] J. E. Kim, Phys. Rev. Lett. **43** 103 (1979).

[41] M. A. Shifman, A. I. Vainshtein, and V. I. Zakharov, Nucl. Phys. **B166**, 493 (1980).

[42] M. Dine, W. Fischler, and M. Srednicki, Phys. Rev. D **104B**, 199 (1985).

[43] K. Choi, Phys. Rev. D **62**, 043509 (2000).

[44] http://www.streakwave.com/mmSWAVE1/Video/ANT-DS-FG16397.pdf

[45] http://www.thinksrs.com/downloads/PDFs/Manuals/SR530m.pdf

[46] Zwicky. F, Helvetica Phy. Acta 6, 110âĂŞ127 (1933).

[47] V. Rubin and W. K. Ford, Astrophysical J. 159, 379 (1970).

[48] V. Rubin, N. Thonnard and W. K. Ford, Astrophysical J. 238, 471 (1980).

[49] R. D. Peccei and H. R. Quinn, Phy. Rev. Lett. 38, 25 (1977).

[50] R. D. Peccei and H. R. Quinn, Phy. Rev. D 16, 6, 1791 (1977).

[51] R. Cameron et al. , Phys. Rev. D 47, 3707 (1993).

[52] E. Zavattini et al. (PVLAS Collaboration), Phys. Rev. Lett. 96, 110406 (2006).

[53] A.S.Chou et al. (GammeV Collaboration), Phys. Rev. Lett. 100, 080402 (2008).

[54] A.Afanasev et al. (LIPSS Collaboration), Phys. Rev. Lett. 101, 120401 (2008).

[55] P. Mohanmurthy, arxiv:1310.6340 (2012).

[56] I. P. Karabekov, R. RosSManith, Proc. of the 1993 PAC, Washington, v. 1, p. 457 (1993).

[57] A. A. Sokolov, N. P. Klepikov and I. M. Ternov, JETF 23, 632 (1952).

[58] J. Allison et. al., IEEE Trans. in Nucl. Science 53, 270 (2006).

[59] I. M. Ternov, Physics - Uspekhi 38, 409 (1995).

[60] P. Mohanmurthy and D. Dutta, arXiv:1309.6711 (2013).

[61] P. Mohanmurthy and D. Dutta, arXiv:1309.2988 (2013).

[62] http://www.pco.de/fileadmin/user_upload/pco-manuals/MA_PCOEDGE_V210.pdf

[63] G. L. Orlandi et. al., Proceedings of IBIC2012, http://ibic12.kek.jp/prepress/papers/mopb82.pdf (2012).

[64] SwissFEL Conceptual Design Report, PSI Bericht Nr. 10-04 (2012).

[65] M. Pedrozzi et al., FEL2011 Free Electron Laser Conference, Shanghai, China, 22-26 (2011).

[66] T. Schietinger, LINAC12 XXVI Linear Accelerator Conference, Tel-Aviv, Israel (2012).

[67] F.Loehl et. al., Phys. Rev. Lett., Volume 104, Issue 14, 144801 (2010).

[68] M. Negrazus, et. al., IEEE Transactions on Applied Superconductivity Vol. 22, Issue 3 (20 11).

[69] E.C. Aschenauer et. al., arxiv:1409.1633 (2014).

[70] Martin Nikl, Meas. Sci. Technol. 17, R37 (2006).

Appendix C

Units

Symbol	Description
T	Unit Multiplier: Tera, 10^12
G	Unit Multiplier: Giga, 10^9
M	Unit Multiplier: Mega, 10^6
k	Unit Multiplier: kilo, 10^3
d	Unit Multiplier: centi, 10^{-1}
c	Unit Multiplier: centi, 10^{-2}
m	Unit Multiplier: milli, 10^{-3}, Unit: meter
μ	Unit Multiplier: micro, 10^{-6}
n	Unit Multiplier: nano, 10^{-9}
p	Unit Multiplier: pico, 10^{-12}
f	Unit Multiplier: femto, 10^{-15}
Hz	Unit: Hertz
eV	Unit: electron-Volt
s	Unit: second
B	Unit: Bell
V	Unit: Volt
Ω	Unit: Ohm
A	Unit: Ampere

Appendix D

Extra Figures
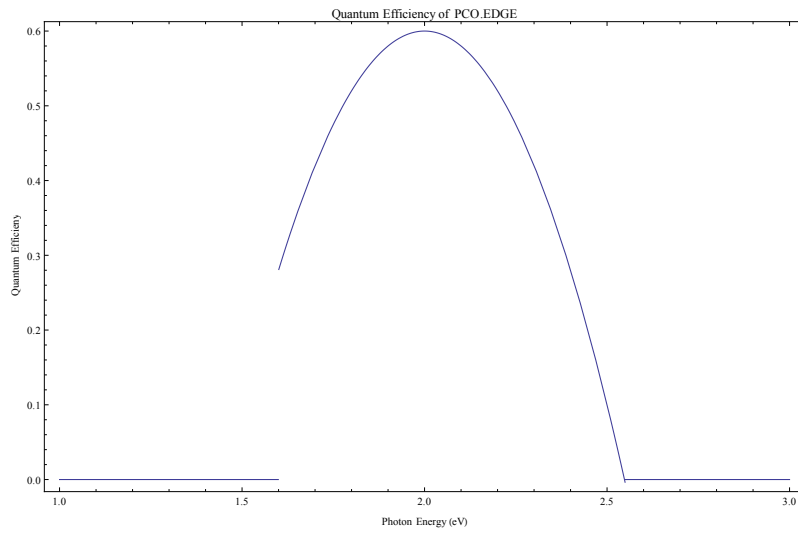
Figure D-1: *Section* **5.4.3** : Plot showing the quantum efficiency of the PCO ™ Edge [62] CCD camera.
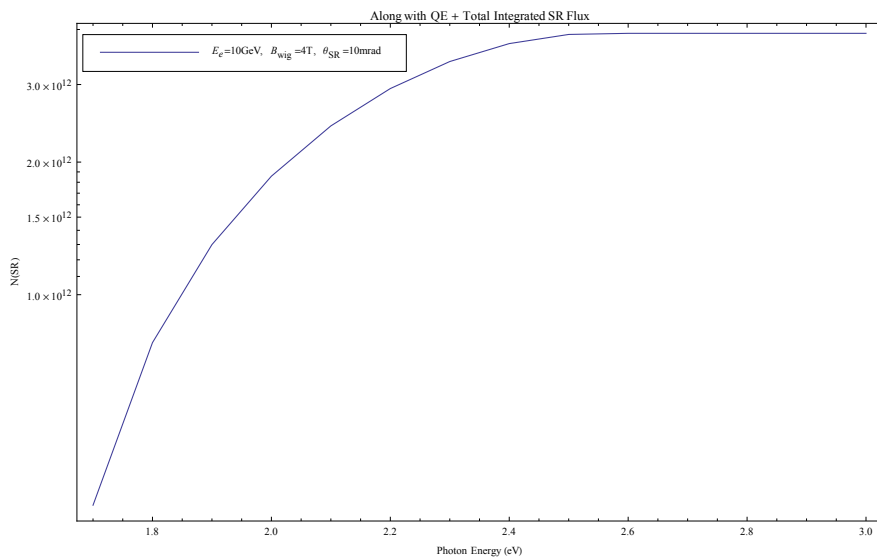
Figure D-2: *Section* **5.4.3** : Plot showing the spectra of total effective flux available from scintillation photons generated by a scintillator upon which SR photons generated at the 4 T wiggler magnet by a 10 GeV electron beam are incident.

List of Figures

List of Tables

Glossary

ALP Axion like particle.

ALPS Axion Like Particle Search.

BAM Beam Arrival Monitor.

BPM Beam Profile Monitor.

BPoM Beam Position Monitor.

BSM Beyond Standard Model.

CAST CERN Axion Solar Telescope.

CCD Charged Coupled Device.

CDMS Cryogenic Dark Matter Search.

C.L Confidence Level.

CP Charge-Parity.

CPT Charge Parity Time.

DPPH Di-Phenyl Picryl Hydrazyl.

EIC Electron Ion Collider.

eRHIC Electron Relativistic Heavy Ion Collider.

FEL Free Electron Laser.

Fermilab Fermi National Accelerator Laboratory.

GammeV γ-eV.

IC Ionization Chamber.

INFN Istituto Nazionale di Fisica Nucleare.